

Leakage-Corrected Discontinuity Factors for a Second-Generation
Th-Pu Pressure-Tube SCWR

by

Katarzyna Carisse

A Thesis Submitted in Partial Fulfillment
of the Requirements for the Degree of

Master of Applied Science

in

The Faculty of Energy Systems and Nuclear Science

Nuclear Engineering

University of Ontario Institute of Technology

August 2014

© Katarzyna Carisse, 2014

Abstract

The neutron flux throughout a reactor core should be calculated, ideally, by solving the neutron transport equation for a highly detailed geometric model of the core. Since this is computationally impractical, approximate node-homogenized models have historically been used whereby neutronic properties are averaged over cartesian parallelepipedic regions called nodes. This process is referred to as homogenization. The simplest homogenization procedure is known as standard homogenization. Standard homogenization calculates node-homogenized cross sections as flux-weighted averages over the volume of each node. It uses an approximate spatial flux distribution obtained from single-node detailed-geometry calculations that approximate the node-boundary conditions to be reflective. While standard homogenization has been successfully used for CANDU reactors, there exist more advanced homogenization methods such as Generalized Equivalence Theory (GET). GET improves accuracy by allowing the neutron flux in the node-homogenized model to be discontinuous at node boundaries through the use of discontinuity factors. Node-averaged cross sections and discontinuity factors can be obtained from single-node calculations using reflective boundary conditions. To further improve accuracy, non-reflective boundary conditions that approximate the real node-boundary conditions can be used; a process known as leakage correction.

This work explores the use of GET with leakage-corrected cross sections and discontinuity factors for the next-generation PT-SCWR flux calculations. Results show that using GET in conjunction with leakage corrections yields substantial improvements in accuracy over standard homogenization and should be given serious consideration as a method for performing neutronic calculations for PT-SCWR cores.

Keywords: Applied Reactor Physics, Advanced Homogenization, CANDU, PT-SCWR

Acknowledgements

I would like to express my thanks to my research supervisor, Dr. Eleodor Nichita, whose knowledge and patience made this work possible. Thank you for the motivation you gave me to persevere and complete this work.

I am grateful for the support received from my employer, Ontario Power Generation, without which it would not have been possible to continue my studies.

Finally, I would like to acknowledge my husband, mother, father, and brother. Thank you for the moral support you provided during both the highs and lows of completing this work.

Table of Contents

Abstract.....	iii
Acknowledgements.....	iv
Table of Contents.....	v
List of Figures.....	vii
List of Tables.....	viii
List of Acronyms.....	ix
List of Symbols.....	x
1 Introduction.....	1
1.1 Background.....	1
1.2 Objective.....	4
1.3 Document Structure.....	4
2 Modelling Neutron Behaviour.....	5
2.1 Neutron Transport Equation.....	5
2.2 Neutron Diffusion Equation.....	7
2.3 Standard Homogenization.....	9
2.4 Generalized Equivalence Theory.....	13
3 Current Progress in Homogenization Methods.....	20
4 The Pressure-Tube Supercritical-Water-Cooled Reactor.....	25
5 Method.....	29
5.1 Diffusion and Transport Calculations.....	30
5.2 Discretization of the Diffusion Equation with Discontinuity Factors.....	31
5.3 Global-Local Iterative Process.....	42
5.4 Node-Boundary Flux and Current from Full-Core Diffusion Calculation.....	46
5.5 Calculation of Discontinuity Factors.....	47
6 Calculations and Results.....	50
6.1 Description of Code.....	50
6.2 Test Model.....	53
6.2.1 Fuel Node Properties.....	56
6.2.2 Configuration of Test Models.....	58

6.3	Comparison of Calculation Methods.....	60
6.4	Error Estimates.....	62
6.5	Results	64
6.5.1	Configuration 1 (10 exit-burnup nodes)	64
6.5.2	Configuration 2 (2 fresh and 8 exit-burnup nodes)	68
6.5.3	Configuration 3 (5 fresh and 5 exit-burnup nodes)	72
6.5.4	Configuration 4 (8 exit-burnup and 2 fresh nodes)	75
6.5.5	Configuration 5 (10 alternating fresh and exit-burnup nodes)	79
7	Discussion.....	83
8	Conclusions and Future Work.....	89
	REFERENCES.....	90

List of Figures

Figure 1 - Simplified depiction of a CANDU lattice cell.	10
Figure 2 - Depiction of Full-Core Node Homogenization.....	11
Figure 3 - PT-SCWR Reactor Core Conceptual Design (Yetisir et al, 2011).....	26
Figure 4 - Mesh Indexing (Nichita et al, 2007).	32
Figure 5 - Flow Chart of Iterative Calculation Process.	45
Figure 6 - Structure of Iterative Code DFLC2G1D.	51
Figure 7 - PT-SCWR Based Core Model with 11 Nodes.	54
Figure 8 - Depiction of Test Model Nodes within PT-SCWR Core (Yetisir et al, 2011).	55
Figure 9 - Single fuel node model.	57
Figure 10 - Configuration 1 Fast Flux Results.	64
Figure 11 - Configuration 1 Thermal Flux Results.	65
Figure 12 - Configuration 1 Fission Rate Results.....	65
Figure 13 - Configuration 2 Fast Flux Results.	68
Figure 14 - Configuration 2 Thermal Flux Results.	69
Figure 15 - Configuration 2 Fission Rate Results.....	69
Figure 16 - Configuration 3 Fast Flux Results.	72
Figure 17 - Configuration 3 Thermal Flux Results.	73
Figure 18 - Configuration 3 Fission Rate Results.....	73
Figure 19 - Configuration 4 Fast Flux Results.	75
Figure 20 - Configuration 4 Thermal Flux Results.	76
Figure 21 - Configuration 4 Fission Rate Results.....	76
Figure 22 - Configuration 5 Fast Flux Results.	79
Figure 23 - Configuration 5 Thermal Flux Results.	80
Figure 24 - Configuration 5 Fission Rate Results.....	80
Figure 25 - Configuration 5 Fission Rate Results for Every Third Iteration.	88

List of Tables

Table 1 - Properties of Fuel Node in DRAGON.	58
Table 2 - Configuration 1 Errors.	67
Table 3 - Configuration 2 Errors.	70
Table 4 - Configuration 3 Errors.	74
Table 5 - Configuration 4 Errors.	77
Table 6 - Configuration 5 Errors.	81
Table 7 - Effect of Iterations on Thermal Absorption Cross Section and Discontinuity Factors.	86

List of Acronyms

CANDU	CANadian Deuterium Uranium
DF	Discontinuity Factor
GET	Generalized Equivalence Theory
LWR	Light Water Reactor
PT-SCWR	Pressure-Tube Supercritical Water Reactor
RBC	Reflective Boundary Condition
SH	Standard Homogenization

List of Symbols

A	Area
S	Surface
V	Volume
D	Diffusion coefficient
\vec{r}	Position
f	Discontinuity factor
g	Neutron energy group
Σ_a	Absorption cross section
Σ_f	Fission cross section
$\Sigma_{g',g}$	Scattering cross section from neutron energy group g' to group g
Σ_t	Total cross section
ν	Average number of neutrons per fission
χ	Group fission spectrum
Ω	Neutron direction
k_{eff}	Effective multiplication factor, k-effective
Ψ	Heterogeneous flux
Φ	Homogeneous flux
\hat{X}	Homogenization of value 'X'
\vec{J}	Neutron current
α	Albedo boundary condition
γ	Current-to-flux ratio boundary condition

1 Introduction

1.1 Background

For a nuclear reactor to operate safely, process parameters such as fuel temperature and coolant temperature need to be maintained within certain safety limits. To ensure that safety limits of these parameters are not exceeded, the reactor safety systems are designed to trip (shut down) the reactor before the safety limits are reached. The difference between the safety limits and the trip limits is known as the safety margin. However, during normal operation the parameters cannot approach the trip limit, as any spurious fluctuation could induce a costly trip. Consequently, the parameters are maintained within an operating domain, circumscribed by operating limits. The difference between the trip limits and the operating limits defines the operating margin. During accidents, parameters can exceed operating limits but they cannot exceed safety limits. Since safety limits are fixed by physical phenomena (e.g., fuel melting temperature), the sizes of the operating and safety margins are chosen as a trade-off between safety and operational flexibility. The wider the margins, the lower the probability of safety limits being exceeded, but the smaller the operating domain and flexibility in operation.

Process parameters such as fuel and coolant temperature depend directly on the power density distribution in the core which, in turn, is determined by the distribution of the neutron flux. Since these process parameters cannot be measured throughout the core,

they are calculated based on numerical simulations and on measurements of the neutron flux at a limited number of locations in the core. Consequently, margins must take into account not only the inherent variability of processes, but also the finite accuracy with which these parameters can be calculated. It follows that an increased accuracy in predicting the neutron flux has direct positive implications on the operation of the reactor by allowing narrower margins and thus a wider operational domain with positive economic effects. The neutron flux is calculated both for routine core operation and for analysis of accident scenarios. During routine operation, the core configuration of a CANDU reactor changes continuously due to changes in the isotopic composition of the fuel, changes in reactivity-device positions, refuelling, etc. Therefore, the neutron flux (and based on it, fuel and coolant temperatures) must be calculated regularly to ensure process parameters such as coolant and fuel temperatures do not exceed operating limits. In the case of accident analysis, the neutron flux is calculated to ensure that process parameters do not exceed safety limits (i.e., the reactor is tripped before safety limits are reached).

Since the neutron flux needs to be calculated both accurately and frequently, the methods used to calculate it have to be accurate but cannot be excessively computationally-intensive. As a consequence, it is desirable to develop approximate methods of finding the neutron flux in the core which offer reduced computation times with only small penalties in accuracy. One widely-used simplification is to use approximate, node-homogenized, geometrical models whereby neutronic properties are

first averaged over large cartesian parallelepipedic regions called nodes. This process is known as homogenization. The simplest homogenization procedure is referred to as standard homogenization (SH). SH calculates node-homogenized cross sections as flux-weighted averages over the volume of each node using an approximate spatial flux distribution obtained from single-node detailed-geometry calculations that approximate the node-boundary conditions to be reflective. While standard homogenization has been used successfully for CANDU reactors, more advanced homogenization methods such as Generalized Equivalence Theory (GET) also exist. GET improves accuracy by allowing the neutron flux in the node-homogenized model to be discontinuous at node boundaries through the use of discontinuity factors. Node-average cross sections and discontinuity factors can be obtained from single-node calculations using reflective boundary conditions. To further improve accuracy, non-reflective boundary conditions that approximate the real node-boundary conditions can be used; a process known as leakage correction.

With the advent of the next-generation Pressure-Tube Supercritical-Water-Cooled Reactor, the question arises whether SH is adequate and whether advanced homogenization methods are necessary.

1.2 Objective

The objective of this work is to implement GET with leakage-corrected cross sections and discontinuity factors for PT-SCWR flux calculations and determine if an improvement is observed over results obtained using standard homogenization methods.

1.3 Document Structure

The document is structured as follows: Chapter 2 presents the general methodology used for calculating the neutron flux in a nuclear reactor, including standard homogenization and GET. Chapter 3 presents an overview of current advanced-homogenization approaches based on GET and otherwise. Chapter 4 presents the characteristics of the PT-SCWR core. Chapter 5 presents the detailed method to calculate leakage-corrected GET parameters as used in this work. Finally, Chapter 6 presents the results obtained using different homogenization methods, and Chapter 7 presents conclusions and suggestions for future investigations.

2 Modelling Neutron Behaviour

There are several types of interactions that a neutron can experience as it moves through its surroundings. For instance, the neutron might be absorbed into the nucleus of an atom and change it into a new isotope of that element. Another possibility is that the neutron will be absorbed and cause fission, splitting one atom into two new ones. Elastic scattering is yet another possibility, whereby the neutron collides with a nucleus and changes its speed and direction. The probability of a neutron having a certain type of interaction per unit path length is represented by the macroscopic cross section. The standard notation for the macroscopic cross section of a material is Σ_x , where 'x' is the type of interaction of interest. The macroscopic cross section for any material varies depending on the energy of the incoming neutron. To facilitate neutronic calculations, the neutron-energy range is divided into groups. The purpose of energy groups is to discretize the energy dependence of the cross sections and of the flux. In detailed transport calculations, it is desirable to represent as many energy groups as possible in order to achieve high accuracy. A few tens of energy groups are generally required.

2.1 Neutron Transport Equation

The interaction of neutrons with matter in a nuclear reactor is best described by the multigroup transport equation which expresses the neutron balance for neutrons belonging to group g and moving in direction Ω as in Eq. (1):

$$\nabla \cdot [\Omega \Psi_g(\Omega, \vec{r})] + \Sigma_{tg}(\vec{r}) \Psi_g(\Omega, \vec{r}) - \sum_{g'} \int_{\Omega'} \Sigma_{sg' \rightarrow g, \Omega' \rightarrow \Omega}(\vec{r}) \Psi_{g'}(\Omega', \vec{r}) d\Omega' = \frac{1}{k_{eff}} \frac{1}{4\pi} \chi_g \sum_{g'} \int_{\Omega'} \Sigma_{fg'}(\vec{r}) \Psi_{g'}(\Omega', \vec{r}) d\Omega' \quad (1)$$

Where:

$\Psi_g(\Omega, \vec{r})$ represents the angular flux,

Ω' and Ω represent the directions of the incoming and scattered neutron respectively,

χ_g represent the neutron energy-group spectrum,

$\Sigma_{tg}(\vec{r})$ represents the total macroscopic cross section, and

$\Sigma_{sg' \rightarrow g, \Omega' \rightarrow \Omega}(\vec{r})$ represents the scattering macroscopic cross section.

By defining the group integral flux as:

$$\Psi_g(\vec{r}) = \int_{\Omega} \Psi_g(\Omega, \vec{r}) d\Omega \quad (2)$$

and the group neutron current, $\vec{J}_g(\vec{r})$, as:

$$\vec{J}_g(\vec{r}) = \int_{\Omega} \Omega \Psi_g(\Omega, \vec{r}) d\Omega \quad (3)$$

the multigroup transport equation can be re-written as:

$$\nabla \cdot \vec{J}_g(\vec{r}) + \Sigma_{tg}(\vec{r}) \Psi_g(\vec{r}) - \sum_{g'} \Sigma_{sg' \rightarrow g}(\vec{r}) \Psi_{g'}(\vec{r}) = \frac{1}{k_{eff}} \chi_g \sum_{g'} \Sigma_{fg'}(\vec{r}) \Psi_{g'}(\vec{r}) \quad (4)$$

The size and complexity of a reactor precludes the possibility of using the transport equation to determine neutron flux throughout the entire core using a large number of groups and a detailed geometrical representation. Neutronic calculations for a full core are made computationally manageable by reducing the number of energy groups (a

process called group condensation) by approximating the transport equation with the diffusion equation. A simplified, node-homogenized geometry is used whereby neutronic properties are first averaged over large cartesian parallelepipedic regions called nodes (a process known as homogenization).

2.2 Neutron Diffusion Equation

The neutron diffusion equation is an approximation of the neutron transport Boltzmann equation derived using Fick's first Law. In its most general form, Fick's Law states that matter will move from regions of high density to regions of lower density. For neutron diffusion, Fick's first Law states that the neutron current is proportional to the gradient of the (integral) neutron flux. Fick's first Law is simply written as:

$$\vec{J}_g = -D_g \nabla \Psi_g \quad (5)$$

where \vec{J}_g represents the group current, D_g represents the diffusion coefficient, ∇ represents the gradient operator, and Ψ_g represents the neutron group flux. By applying Fick's Law, the multigroup transport equation can be reduced to the multigroup diffusion equation:

$$\nabla \cdot [D_g(\vec{r}) \Psi_g(\vec{r})] + \Sigma_{tg}(\vec{r}) \Psi_g(\vec{r}) - \sum_{g'} \Sigma_{sg' \rightarrow g}(\vec{r}) \Psi_{g'}(\vec{r}) = \frac{1}{k_{eff}} \chi_g \sum_{g'} \Sigma_{fg'}(\vec{r}) \Psi_{g'}(\vec{r}) \quad (6)$$

Just like the transport equation, the diffusion equation expresses the neutron balance, but unlike the transport equation, it makes the additional simplifying assumption that

the flux is only linearly anisotropic. As a consequence, the angular dependence of the neutron flux is absent from the diffusion equation.

For diffusion calculations performed using a node-homogenized model, neutron energy is often divided only into a “fast” and a “thermal” group, typically separated by a threshold energy in the ~1 eV range. Thermal neutrons are created when fast neutrons, born in fission, are slowed down (moderated). They can cause fission, be captured, or leak out from the system. The designation “thermal” is used to indicate that the neutrons are in thermal equilibrium with their surroundings. Fast neutrons are created by fission and, to a small degree, by up-scattering of thermal neutrons. They are lost due to thermalization (down-scattering to the thermal energy group), fission, capture, or leaking out of the system. In a steady state core, the two group diffusion equations for the node-homogenized core are written as:

$$\begin{aligned}
 & -D_1(\vec{r})\nabla^2\Phi_1(\vec{r}) + \hat{\Sigma}_{a1}(\vec{r})\Phi_1(\vec{r}) + \hat{\Sigma}_{12}(\vec{r})\Phi_1(\vec{r}) - \hat{\Sigma}_{21}(\vec{r})\Phi_2(\vec{r}) = \\
 & \frac{1}{k_{eff}} \left[\nu\hat{\Sigma}_{f1}(\vec{r})\Phi_1(\vec{r}) + \nu\hat{\Sigma}_{f2}(\vec{r})\Phi_2(\vec{r}) \right] \quad (7) \\
 & -D_2(\vec{r})\nabla^2\Phi_2(\vec{r}) + \hat{\Sigma}_{a2}(\vec{r})\Phi_2(\vec{r}) + \hat{\Sigma}_{21}(\vec{r})\Phi_2(\vec{r}) - \hat{\Sigma}_{12}(\vec{r})\Phi_1(\vec{r}) = 0
 \end{aligned}$$

where the symbol “^” over the cross sections represents the fact that they are node-homogenized and the symbol Φ is used to denote the flux obtained for the node-homogenized model, usually referred to as the “homogeneous” flux. Conversely, the flux, Ψ , obtained for a detailed-geometry heterogeneous model is referred to as the

“heterogeneous” flux. In Eq. (7) $\nu\hat{\Sigma}_{f1}(\vec{r})\Phi_1(\vec{r})$ and $\nu\hat{\Sigma}_{f2}(\vec{r})\Phi_2(\vec{r})$ represent the neutron production rate densities for fast and thermal fission, respectively.

$\hat{\Sigma}_{a1}(\vec{r})\Phi_1(\vec{r})$ and $\hat{\Sigma}_{a2}(\vec{r})\Phi_2(\vec{r})$: fast and thermal neutron absorption rate density,

$\hat{\Sigma}_{12}(\vec{r})\Phi_1(\vec{r})$ and $\hat{\Sigma}_{21}(\vec{r})\Phi_2(\vec{r})$: scattering rate density from group 1 to 2 and *vice versa*,

$D_1(\vec{r})\nabla^2\Phi_1(\vec{r})$ and $D_2(\vec{r})\nabla^2\Phi_2(\vec{r})$: group-1 and group-2 neutron leakage rate density.

The solution of the diffusion equation provides the neutron flux values and the system eigenvalue, which is commonly referred to as the effective multiplication constant, “k-effective”. The disadvantage of using the diffusion equation is that the simplifying assumptions it relies on tend to break down near boundaries, neutron sources, and strong absorbers. However, for a node-homogenized model, the approximations necessary to derive the diffusion equation are valid. In particular, variations in node-wise macroscopic cross sections are much smaller than the respective variations in cross sections for a detailed-geometry model. The diffusion approximation has historically been acceptable for use in CANDU reactor neutronics modelling.

2.3 Standard Homogenization

The node-homogenized core model is obtained by first subdividing the reactor into cartesian parallelepipedic nodes which are small enough to allow the detailed-geometry transport equation to be solved with no challenge to computational resources. In PWR reactors, each node usually represents a section (several tens of centimetres long) of

one fuel assembly. For CANDU reactor physics analysis, each three-dimensional node contains one fuel bundle and the coolant and moderator which surround it. A two-dimensional cross section (X-Y) of a CANDU node is illustrated in Fig. 1. Such a two-dimensional region containing the fuel channel and surrounding moderator is commonly referred to as a lattice cell.

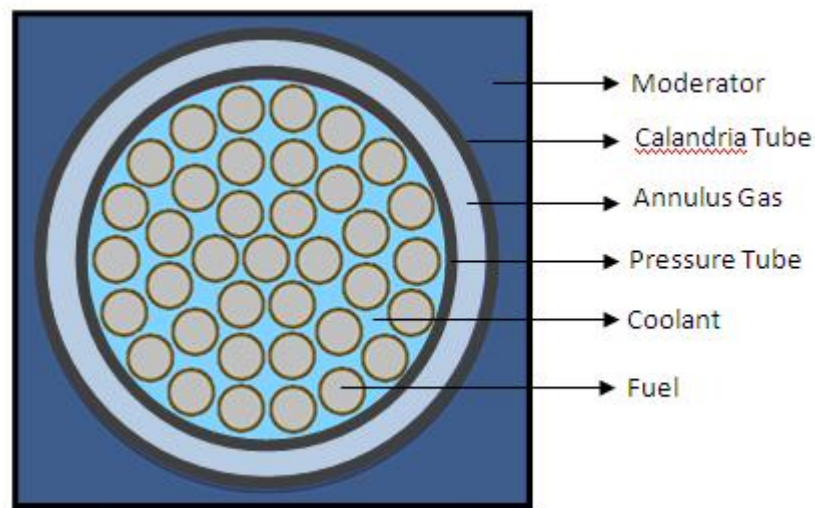


Figure 1 - Simplified depiction of a CANDU lattice cell.

The homogenized macroscopic neutron cross sections for each node are computed by a “lattice” code which solves the transport equation in a few tens of energy groups, condenses them to two groups and, finally, calculates the flux-weighted two-group cross section averages. When solving the transport equation, the true (but unknown) node-boundary conditions are approximated to be reflective. The current industry-standard code for CANDU lattice calculations is WIMS-AECL. To avoid performing transport calculations for each individual node, single-node (lattice cell) homogenized neutronic

parameters are usually first tabulated as a function of fuel burnup and local fuel and coolant temperatures and densities. The macroscopic cross-section values for each node are subsequently found by interpolating in the table using the local fuel burnup, temperatures and densities for the node in question. After this process is complete, the detailed neutronic properties for each individual component of the node are lost; replaced by one set of homogenized neutronic parameters for each node. The totality of the homogenized nodes (4560 for a CANDU-6 reactor) makes up the node-homogenized “full-core” reactor model. The two-group diffusion equation is then solved for this full-core model to obtain the three-dimensional flux distribution and power profile in the core.

The node-homogenization process is depicted in Fig. 2.

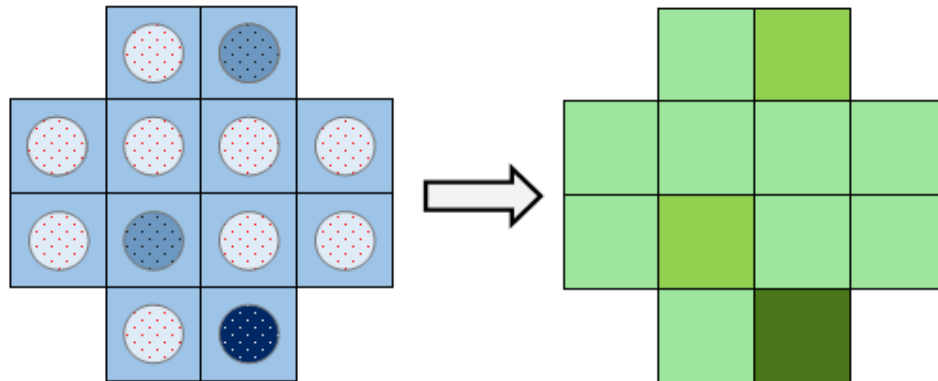


Figure 2 - Depiction of Full-Core Node Homogenization.

In Fig. 2, the left-hand image represents a heterogeneous core model while the right-hand image shows the same model after node-homogenization has been completed.

The different shades inside the circular fuel bundles in the heterogeneous core represent different fuel burnups. Similarly, different shades for the square regions in the homogenized model correspond to different burnups. In the homogenized model, the detailed geometry of the fuel bundle has also been replaced with a single region, representing the homogenized node.

The process described above for obtaining a single set of macroscopic cross sections for each node is known as Standard Homogenization (SH), and it is the accepted practice for CANDU reactor physics calculations. The solution of the flux obtained using SH is known as the homogeneous flux, due to the use of homogenized parameters. The flux solution which would theoretically be obtained from solving the transport equation over the entire core is the heterogeneous flux. Standard homogenization approximates the true heterogeneous flux at the node level by assuming node boundary conditions to be reflective.

Typically, using the node-homogenized neutronic parameters to solve the diffusion equation for flux produces adequate results for CANDU reactors (i.e., a reasonably low bundle-power error). For highly heterogeneous configurations, the results from SH tend to give poorer results due largely to the breakdown of SH approximations near regions with significant changes in neutron density, such as strong absorbers or sources. Due to this, significant work has been performed in the field of improving the SH technique for heterogeneous reactor designs.

2.4 Generalized Equivalence Theory

Ideally, the homogeneous flux resulting from the diffusion equation should preserve the node-integrated reaction rates, surface leakage, and eigenvalue of the whole core.

Standard homogenization does not give any assurances, beyond empirical evidence, that this is the case. To accomplish the objective of preserving node-integrated quantities, an “equivalence theory” was developed by Koebke (1978). This was further expanded upon with a technique termed Generalized Equivalence Theory (GET) by Smith (1986). The main feature of GET is the introduction of a new parameter for use in node-homogenized diffusion calculations termed the flux “discontinuity factor”.

As mentioned previously, GET aims to define the neutronic properties of the node-homogenized model such that the node-averaged quantities (group neutron flux and reaction rates) obtained using the node-homogenized model are equal to those obtained using the heterogeneous model. Additionally, the neutron leakage through each heterogeneous-node face should equal the neutron leakage through the corresponding homogeneous-node face. With that in mind, it is useful to write the node-integrated form of the neutron balance equation as expressed by both the heterogeneous and the homogeneous models. For the heterogeneous model, the node-integrated balance equation for cartesian node i can be written as:

$$\begin{aligned} & \sum_k \bar{J}_{gik} u_k A_{ik} + \int_{V_i} \sum_{Tg} (\vec{r}) \Psi_g(\vec{r}) dV - \sum_{g'} \int_{V_i} \sum_{Sg' \rightarrow g} (\vec{r}) \Psi_{g'}(\vec{r}) dV = \\ & \frac{1}{k_{eff}} \sum_{g'} \int_{V_i} \chi_g \nu \sum_{fg'} (\vec{r}) \Psi_{g'}(\vec{r}) dV \end{aligned} \quad (8)$$

In the above equation, subscript k indexes the faces of cartesian node i . In three dimensions, there are six faces. In two dimensions the number of faces is reduced to four and in one dimension the number of faces is only two. A_{ik} represents the area of face k in node i and u_k is the sign of the dot product between the outward normal to face ik and the versor of the cartesian axis to which the face is perpendicular. The average face current, \bar{J}_{gik} , is defined as:

$$\bar{J}_{gik} = \frac{1}{A_{ik} S_k} \int_{S_k} \bar{J}_g(\vec{r}) d\vec{S} \quad (9)$$

Where S_k is the surface of face k .

For the homogeneous model, the node-integrated balance equation is written as:

$$\begin{aligned} & \sum_k \hat{J}_{gik} u_k A_{ik} + \hat{\Sigma}_{Tgi} \int_{V_i} \Phi_g(\vec{r}) dV - \sum_{g'} \hat{\Sigma}_{sig' \rightarrow g} \int_{V_i} \Phi_{g'}(\vec{r}) dV = \\ & \frac{1}{\hat{k}_{eff}} \sum_{g'} \hat{\chi}_g \nu \hat{\Sigma}_{fg'} \int_{V_i} \Phi_{g'}(\vec{r}) dV \end{aligned} \quad (10)$$

Where V_i is the volume of node i .

The face-average current, \hat{J}_{gik} , is defined as:

$$\hat{J}_{gik} = \frac{1}{A_{ik} S_k} \int_{S_k} D_{gi} \nabla \Phi_g(\vec{r}) d\vec{S} \quad (11)$$

The equality of the heterogeneous and homogenous node-average flux requires that:

$$\int_{V_i} \Phi_g(\vec{r}) d\vec{r} = \int_{V_i} \Psi_g(\vec{r}) dV \quad (12)$$

The equality of the heterogeneous and homogeneous node-average reaction rates require that:

$$\hat{\Sigma}_{gi} \int_{V_i} \Phi_g(\vec{r}) d\vec{r} = \int_{V_i} \Sigma_g(\vec{r}) \Psi_g(\vec{r}) d\vec{r} \quad (13)$$

The equality of heterogeneous and homogenous leakage rates require that:

$$\hat{J}_{gik} = \bar{J}_{gik} \quad (14)$$

It follows that each node-homogenized cross section must be defined as:

$$\hat{\Sigma}_{i,g} \equiv \frac{\int_{V_i} \Sigma_g(\vec{r}) \Psi_g(\vec{r}) dV}{\int_{V_i} \Phi_g(\vec{r}) dV} \quad (15)$$

Since the average fluxes are also equal, it also follows that the node-homogenized cross section can be defined as simply the flux-weighted average of the heterogeneous cross section:

$$\hat{\Sigma}_{i,g} \equiv \frac{\int_{V_i} \Sigma_g(\vec{r}) \Psi_g(\vec{r}) dV}{\int_{V_i} \Psi_g(\vec{r}) dV} \quad (16)$$

Once the homogenized cross sections are calculated according to Eq. (16) and homogeneous node-boundary currents are defined as being equal to the heterogeneous ones, a well-posed diffusion problem can be defined in each node. The resulting single-node homogeneous flux in each node will satisfy:

$$\begin{aligned} & \sum_k \hat{J}_{gik} u_k A_{ik} + \hat{\Sigma}_{tgi} \int_{V_i} \Phi_{ig}(\vec{r}) dV - \sum_{g'} \hat{\Sigma}_{sig' \rightarrow g} \int_{V_i} \Phi_{ig'}(\vec{r}) dV = \\ & \frac{1}{k_{eff}} \sum_{g'} \hat{\chi}_g \nu \hat{\Sigma}_{fg'} \int_{V_i} \Phi_{ig'}(\vec{r}) dV \end{aligned} \quad (17)$$

Where $\Phi_{ig}(\vec{r})$ represents the single-node homogeneous flux.

Moreover, the homogeneous node-integrated homogeneous flux will equal the node-integrated heterogeneous flux. That can be seen by the following argument. First, Eq. (17) is re-written as:

$$\left(\frac{1}{k_{eff}} \sum_{g'} \hat{\chi}_g \nu \hat{\Sigma}_{fg'} + \hat{\Sigma}_{sig' \rightarrow g} - \hat{\Sigma}_{tgi} \delta_{gg'} \right) \int_{V_i} \Phi_{ig'}(\vec{r}) dV = \sum_k \hat{J}_{gik} u_k A_{ik} \quad (18)$$

Which is a non-singular linear system in unknowns $\int_{V_i} \Phi_{ig'}(\vec{r}) dV$ and, therefore, has a unique solution.

Equation (18) is processed by multiplying and dividing each volume term by an integral of the type $\int_{V_i} \Psi_g(\vec{r}) dV$:

$$\begin{aligned}
& \sum_k \bar{J}_{gik} u_k A_{ik} + \frac{\int_{V_i} \Sigma_{tg}(\vec{r}) \Psi_g(\vec{r}) dV}{\int_{V_i} \Psi_g(\vec{r}) dV} \int_{V_i} \Psi_g(\vec{r}) dV - \\
& \sum_{g'} \frac{\int_{V_i} \Sigma_{sg' \rightarrow g}(\vec{r}) \Psi_{g'}(\vec{r}) dV}{\int_{V_i} \Psi_{g'}(\vec{r}) dV} \int_{V_i} \Psi_{g'}(\vec{r}) dV = \\
& \frac{1}{k_{eff}} \sum_{g'} \frac{\int_{V_i} \chi_g \nu \Sigma_{fg}(\vec{r}) \Psi_{g'}(\vec{r}) dV}{\int_{V_i} \Psi_{g'}(\vec{r}) dV} \int_{V_i} \Psi_{g'}(\vec{r}) dV
\end{aligned} \tag{19}$$

and further processed to outline the homogeneous cross sections:

$$\begin{aligned}
& \sum_k \bar{J}_{gik} u_k A_{ik} + \hat{\Sigma}_{tgi} \int_{V_i} \Psi_g(\vec{r}) dV - \sum_{g'} \hat{\Sigma}_{sig' \rightarrow g} \int_{V_i} \Psi_{g'}(\vec{r}) dV = \\
& \frac{1}{k_{eff}} \sum_{g'} \hat{\chi}_g \nu \hat{\Sigma}_{f ig'} \int_{V_i} \Psi_{g'}(\vec{r}) dV
\end{aligned} \tag{20}$$

Finally, the terms depending on currents are isolated on the right:

$$\left(\frac{1}{k_{eff}} \sum_{g'} \hat{\chi}_g \nu \hat{\Sigma}_{f ig'} + \hat{\Sigma}_{sig' \rightarrow g} - \hat{\Sigma}_{tgi} \delta_{gg'} \right) \int_{V_i} \Psi_{g'}(\vec{r}) dV = \sum_k \bar{J}_{gik} u_k A_{ik} \tag{21}$$

The above is also a non-singular linear system in unknowns $\int_{V_i} \Psi_{g'}(\vec{r}) dV$ which has a unique solution.

Since the homogeneous and heterogeneous face currents are equal by construction, the two linear systems have the same coefficients, the same source terms, and consequently the same solution. It follows that:

$$\int_{V_i} \Phi_{ig}(\vec{r}) dV = \int_{V_i} \Psi_{ig}(\vec{r}) dV \quad (22)$$

The overall core-wide homogeneous flux can subsequently be defined as being piecewise equal to the single-node homogeneous flux in each node, that is:

$$\Phi_g(\vec{r}) = \Phi_{ig}(\vec{r}) \quad \vec{r} \in V_i \quad (23)$$

The homogeneous flux defined as above is piecewise continuous but may not be truly continuous at node interfaces. Since the heterogeneous flux satisfies Eq. (21), and since the heterogeneous flux is continuous at node interfaces, the “discontinuity factors” can be defined as the ratio between the face-average homogeneous flux and the face-average heterogeneous flux:

$$f_{gik} = \frac{\bar{\Psi}_{gik}}{\bar{\Phi}_{gik}} \quad (24)$$

Once the discontinuity factors have been defined, the continuity of the heterogeneous flux across node boundaries can be written using the homogeneous flux as:

$$\Phi_{gik} f_{gik} = \Phi_{gjk'} f_{gjk'} \quad (25)$$

Where face ik and jk' represents the common face of nodes i and j .

It follows that the full-core homogeneous flux can also be defined as the solution to Eq. (21) with flux continuity conditions across node interfaced being replaced by the “discontinuity” conditions expressed by Eq. (25).

In GET, the homogenized diffusion coefficient, \hat{D}_{ig} , can, in principle, be arbitrary and is often defined as:

$$\hat{D}_{ig} \equiv \frac{\int_{V_i} D_g(\vec{r}) \Psi_g(\vec{r}) dV}{\int_{V_i} \Psi_g(\vec{r}) dV} \quad (26)$$

The challenge in implementing discontinuity factors is that the heterogeneous neutron flux, Ψ_g , is not known beforehand for the core model being used. To circumvent this problem, the heterogeneous flux is normally determined with a single node calculation assuming reflective (that is, zero current) boundary conditions. Thus,

$$\vec{J}\hat{n} = 0 \quad (27)$$

for each face of the single node, where \hat{n} is the unit normal to the face of the boundary.

With reflective boundary conditions, the calculation of homogenized cross sections is identical to that used in SH:

$$\hat{\Sigma}_g \equiv \frac{\int \Sigma_g(\vec{r}) \Psi_g^0(\vec{r}) d^3\vec{r}}{\int \Psi_g^0(\vec{r}) d^3\vec{r}} \quad (28)$$

Where the “0” superscript here denotes the use of reflective boundary conditions. The reflective boundary condition is an assumption and its accuracy will vary from node to node in the core. If the surrounding nodes are similar to the node in question, the reflective boundary condition assumption tends to produce satisfactory results. Factors such as strong absorbers or sources close to the node will significantly challenge the reflective boundary condition assumption.

3 Current Progress in Homogenization Methods

A number of researchers have addressed the issue of compensating for the effect of neighbouring nodes (commonly called the “environmental effect”) while performing heterogeneous-node calculations. One method suggested by Aragoes and Ahnert (1986) was to iterate between full-core calculations and heterogeneous single node calculations. This allows for the boundary conditions on each heterogeneous node to be updated with information from the whole-core diffusion run after each iteration. The method has been shown to be effective in PWR modelling but has not yet been applied to heavy-water reactors.

In order to save the cost of performing the single-node calculations for each iteration, Rahnema (1989) took the approach of determining the homogenized cross sections as a function of the boundary condition. An improvement on this method was the work of Kim and Cho (1993), which used an improved global local iteration technique to account for the environmental effect. The homogenized parameters at each cross section iteration were corrected using the variational principle described by Pomraning (1967).

The technique of rehomogenization was introduced by Smith (1994). The heterogeneous flux between nodes was obtained by modulating the heterogeneous zero-current shape with the homogeneous flux shape. However, the discontinuity factor cannot be corrected between iterations by using this technique. Additionally,

accurate intranodal shapes are a requirement of obtaining good estimates of the homogenized cross sections.

Rahnema and Nichita (1997) proposed a method which uses the global-local iteration technique and calculates cross sections at each iteration step with a linear interpolation scheme. Interpolation is performed on a series of corrections to the homogenized parameters precomputed during the heterogeneous node calculation. The cross sections and discontinuity factors were independently related to the surface current-to-flux ratio of each surface. This method was demonstrated for a BWR reactor and in diffusion-theory only. It corrected both the homogenized cross sections and the discontinuity factor due to the actual boundary conditions of each node.

The approach of tabulating the effects of differing neighbour nodes was also shown to be effective by Clarno and Adams (2003). In this work, quasi-diffusion methods were used with interpolation of neighborhood effects in MOX and UO₂ fuel assemblies.

Another work, by Merk and Rohde (2011) suggested placing the reflective boundary condition in the centre of each fuel element. The two group diffusion equations were then solved as an external source problem, which was implemented successfully on a homogeneous system. The diffusion equations were solved analytically and iterations were not required, since all values were prepared during the calculation of cross sections. This method was also demonstrated to be successful on a heterogeneous system containing a mix of MOX and UO₂ fuel in a PWR.

The use of neighbouring-node corrected discontinuity factors for pin-by-pin diffusion calculations in a light-water reactor was addressed by Herrero *et al* (2012). This work suggested a methodology to consider the neighbourhood effect based on the Analytic Coarse-Mesh Finite Difference (ACMFD) method for the multi-group diffusion equation. This work developed computational methods for the generation of multi-group cross-section libraries with multifunctional dependencies for use in pin-by-pin transient calculations. A functional-fitting of the discontinuity factors based on the analytical terms in the ACMFD calculation was created for the multi-group diffusion equation. This was shown to yield promising results and to be suitable for pin-by-pin diffusion calculations.

Another method to improve upon SH is Superhomogenization (SPH). SPH uses SPH factors, which are applied to each average macroscopic cross section to allow the corresponding node-integrated reaction rate for the homogenized node to exactly match the one for the heterogeneous node (Hebert, 1993). SPH tends to produce satisfactory results for one dimensional problems or for highly symmetrical problems with more dimensions, but can sometimes run into difficulties for severely heterogeneous configurations (Berman, 2013). An iterative, semi-homogenized (ISH) approach was suggested by Berman (2013). In this method, a finite number of diffusion coefficients was introduced, and each node is treated as a “semi-homogeneous” material. The diffusion coefficients were used to preserve the node-integrated reaction rates to those from heterogeneous results. All other node parameters, such as the cross

sections, remained homogeneous. One of the limitations of this approach is that the reactor must be divided into fine meshes for results to be meaningful. This presents an increase in computational time, as smaller mesh divisions create more nodes over which to perform single-node calculations. Additionally, in highly asymmetric cases, the system eigenvalue between the ISH calculation and the reference calculation is relatively high.

Presently, most light water reactors (LWR) use two energy groups and coarse meshes with reflective boundary conditions for reactor analysis. This methodology has reasonably accurate results for LWR designs. However, these advanced homogenization techniques have not been used for CANDU reactors since the benefits become more apparent in highly heterogeneous reactor designs, such as the Pressurized Water Reactor (PWR). Gomes (2009) emphasized the importance of using discontinuity factors in cores with heterogeneous fuel assemblies. This was discussed in particular for cores with MOX and low-enriched uranium (LEU) core designs, where techniques must be used to counter the effects of homogenization. Without consideration for these corrections, the power errors resulting from using diffusion codes were shown to be unacceptably high. A correlation between power error and discontinuity factor was found. For PWR and BWR configurations, Dall'Osso (2006) emphasized the importance of using discontinuity factors to preserve mesh-integrated reaction rates.

Based on the acceptance of improved homogenization on LWR reactors, the applicability of Standard Homogenization should be re-evaluated for future CANDU designs. If the CANDU design is altered to tend towards a more heterogeneous configuration, the use of homogenized parameters to solve the diffusion equation may no longer be sufficient.

4 The Pressure-Tube Supercritical-Water-Cooled Reactor

The Generation IV International Forum (GIF) was established in 2001 as an international cooperative group with the mandate of researching next-generation reactor designs.

Canada is one of the (currently) thirteen member nations participating in the GIF forum.

The next generation (Gen IV) CANDU reactor being pursued by the GIF is the

Supercritical Water Cooled Reactor (SCWR). The SCWR is an advanced reactor design. It

is theoretically capable of increasing the thermal efficiency of the steam cycle to ~45-

50% by operating above the thermodynamic critical point of water (647 K and 22 MPa).

This is a significant improvement on the current cycle efficiency, which is approximately 30-35% for CANDU reactors.

Currently, the SCWR design is in the conceptual phase, and multiple possibilities for its

design are being explored. Both a pressure-tube and a pressure-vessel design have

been considered for the core (McDonald, 2011). In the pressure vessel design the fuel,

moderator, and coolant are contained together in a vessel which is capable of providing

the required pressure-boundary. Alternatively, the pressure-tube SCWR consists of

many pressurized cylindrical tubes holding the fuel and coolant separate from the

moderator. The pressure tube concept has been used successfully in all previous

CANDU designs. For this work, the pressure-tube SCWR concept will be considered. The

PT-SCWR reactor consists of a vertical cylindrical vessel containing heavy-water

moderator at low temperature and near-atmospheric pressure. Light water is used as

the coolant, which saves the cost of using heavy water. The disadvantage of light water

is the penalty to the neutron economy, since light water has a higher neutron absorption cross section than heavy water. The vessel contains a rectangular array of 336 parallel fuel channels oriented axially as shown in Fig. 3 below (Yetisir *et al*, 2011).

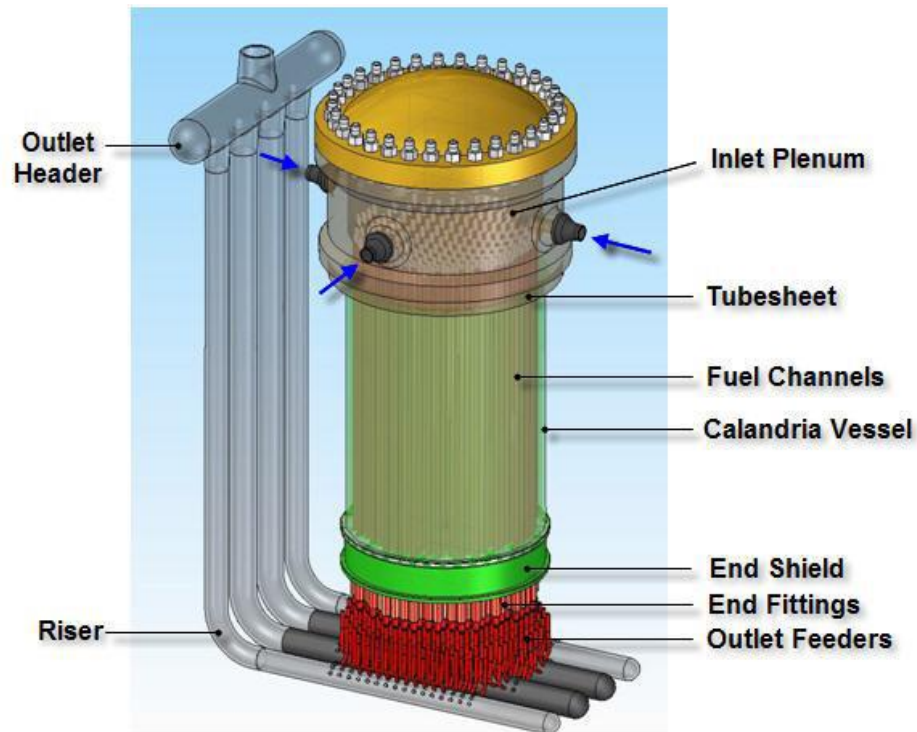


Figure 3 - PT-SCWR Reactor Core Conceptual Design (Yetisir *et al*, 2011).

For the second-generation design of the PT-SCWR, each fuel channel consists of a zirconium alloy pressure tube lined by a ceramic thermal insulator (yttrium-stabilized zirconia) which holds the fuel assembly. Fuel assemblies consist of 78 five metre-long fuel rods arranged in three concentric annuli and a central zirconium oxide element. The ceramic thermal insulator ensures that the temperature of the moderator remains relatively low. The distance between channels (lattice pitch) is 25.0 cm. The fuel is a combination of thorium oxide and plutonium oxide, with plutonium representing

approximately 12% by heavy element weight. The initial isotopic composition of plutonium is taken to correspond to 44 kWd/kg PWR spent fuel (originally enriched to 4.1%). The choice of using thorium as part of the fuel mix increases the sustainability of the PT-SCWR, as thorium is thought to be about three times more abundant than uranium.

Another feature of the PT-SCWR which departs from the current CANDU design is that the pressure tube is in direct contact with the moderator. This is made possible by a ceramic insulator which is located on the inside surface of the pressure tube, and prevents the moderator from overheating due to the hot coolant. Additionally, the pressure tube material itself is protected from the supercritical coolant water. If the insulator were not present, a zirconium alloy could not be used for the pressure tube material as it may not withstand the environment of the supercritical coolant.

The use of supercritical water as a coolant precludes the possibility of performing online refuelling. The pressures and temperatures of the fuel channels are too high to risk attempting a seal of the fuelling machine to the channel while operating at full power. Thus, the refuelling strategy of the PT-SCWR is expected to be batch refuelling offline, as it is for many other reactors (e.g., the PWR). Additionally, the penalty to neutron economy from using light water coolant and the use of batch refuelling will require the PT-SCWR to have enriched fuel. This is a significant departure from operating CANDU reactors, which do not require fuel enrichment.

The differences in core design between currently operating CANDU reactors and the proposed PT-SCWR are responsible for significant differences in neutronic behaviour. The radial power distribution is uneven in the PT-SCWR core because of the higher variations in fuel burnup. Early neutronic calculations performed for the CANDU-SCWR have thus far used methods employed by current CANDU reactors. The lattice code WIMS and the diffusion code RFSP have been utilized for neutronic analysis to this point. This code combination uses standard homogenization techniques without employing interface discontinuity factors like for existing PWRs and BWRs. No lattice-cell correction for the effect of neighbouring nodes has been considered when calculating homogenized parameters. As previously discussed, heterogeneous designs such as the PWR have already been demonstrated to require improvements on standard homogenization. Thus, the question arises on whether or not the implementation of such improvements is warranted on the PT-SCWR. According to Shen (2012a), the current standards of neutronic analysis for CANDU reactors is not sufficient for PT-SCWR calculations. In that work, a two dimensional benchmark problem of the PT-SCWR design was setup to assess the validity of traditional core analysis methods. It was found that current methods are not sufficient to capture the spectral change or the environmental effect for the PT-SCWR core. The power error resulting from application of standard homogenization to the PT-SCWR was determined to be unacceptably high. The need for a different approach to neutronic calculations for the PT-SCWR core is, therefore, evident.

5 Method

As mentioned in the introduction, the purpose of this work is to explore the application of GET to PT-SCWR configurations. The GET implementation starts with exact values of the node-homogenized parameters as described by Eq. (16) and (24), which can be obtained if the exact heterogeneous flux is known or, equivalently, if the exact heterogeneous-node boundary conditions are known. The homogeneous flux inside the node can be found by solving the diffusion equation using the homogenized cross sections and fixed-current (equal to the exact, heterogeneous current) boundary conditions.

Since the full-core heterogeneous flux is not known in advance for any real practical case, it has to be approximated. The simplest approximation is to use a reflective boundary condition (RBC) on the heterogeneous-node boundaries. Discontinuity factors obtained using RBC are also called Assembly Discontinuity Factors (ADFs), because a node usually corresponds to a fuel assembly. ADFs can be shown to be equal to the ratio of the face-averaged heterogeneous flux to the node-averaged heterogeneous flux:

$$f_{sg}^0 = \frac{\bar{\Psi}_{sg}^0}{\bar{\Psi}_{vg}^0} \quad (29)$$

where the “0” subscript denotes zero-current boundary conditions. The corresponding homogenized cross sections are calculated as:

$$\hat{\Sigma}_g \equiv \frac{\int_V \Sigma_g(\vec{r}) \Psi_g^0(\vec{r}) d^3\vec{r}}{\int_V \Psi_g^0(\vec{r}) d^3\vec{r}} \quad (30)$$

A better approximation of the heterogeneous flux can be obtained by using improved boundary conditions on the node boundaries. Approximate node boundary conditions can be obtained from a full-core diffusion calculation performed using RBC node cross sections and ADFs. The calculated node boundary conditions can be used to calculate a new, non-RBC, set of node-homogenized cross sections and discontinuity factors. The newly obtained cross sections and discontinuity factors can be used in a subsequent core calculation which, in turn, provides new node boundary conditions. The iterative process can be continued until a pre-defined convergence criterion is met which, for BWR lattices usually occurs in fewer than 10 iterations (Rahnema and Nichita, 1997). Further details of this process are presented in subsequent sections.

5.1 Diffusion and Transport Calculations

Two distinct codes were used to facilitate transport and diffusion calculations while implementing GET on PT-SCWR neutronic calculations. The lattice code DRAGON (Marleau *et al*, 2012), developed at École Polytechnique de Montréal, was used to perform the transport calculations. DRAGON can solve the multigroup transport equation using the collision probabilities (CP) method or the method of characteristics (MOC). Two-group CP method is used for this work. DRAGON can use general boundary

conditions in the form of group albedos, α_g , which are defined as the ratio of the outgoing current to the incoming current:

$$\alpha_g \equiv \frac{J_g^{out}}{J_g^{in}} \quad (31)$$

Two-group diffusion calculations are performed using DISDIF3D, a code previously developed at UOIT (Nichita *et al*, 2007). DISDIF3D is capable of solving the three-dimensional two-group diffusion equation using the mesh-centered finite differences (MCFD) method. It can use discontinuity factors at node boundaries and general system boundary conditions specified as either current-to-flux ratio, fixed current, or fixed flux.

5.2 Discretization of the Diffusion Equation with Discontinuity Factors

This section describes the mesh-centred finite-difference discretization of the multigroup diffusion equation when flux is assumed to be discontinuous on mesh boundaries. To do so, the domain is divided into parallelepipedic mesh boxes using a three-dimensional rectangular grid. Each mesh box is indexed with the triplet (i, j, k) , where i , j , and k , correspond to directions x , y , and z respectively. The side lengths of each mesh box are h_{xi} , h_{yj} , and h_{zk} . A boundary between two meshes is denoted by a "1/2" in the index corresponding to the direction to which the boundary is perpendicular. For example, the boundary between node (i, j, k) and node $(i, j + 1, k)$ is denoted by $(i, j + 1/2, k)$. The mesh indexing scheme is illustrated in Fig. 4.

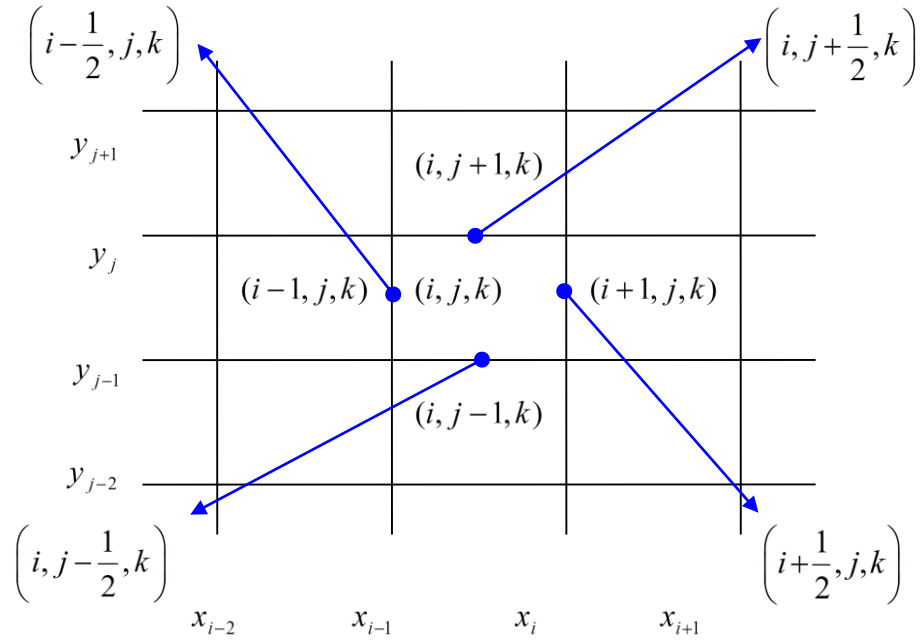


Figure 4 - Mesh Indexing (Nichita et al, 2007).

The grid planes perpendicular to the x -axis intersect it at points x_i ($i=0,1,2,\dots$). The grid planes perpendicular to the y -axis, intersect it at points y_j ($j=0,1,2,\dots$). The grid planes perpendicular to the z -axis intersect it at points z_k ($k=0,1,2,\dots$). It follows that

$$\begin{aligned}
 h_{xi} &= x_i - x_{i-1} \\
 h_{yj} &= y_j - y_{j-1} \\
 h_{zk} &= z_k - z_{k-1}
 \end{aligned}
 \tag{32}$$

It should be noted that the indexing of x , y , and z axis points is somewhat inconsistent with the indexing of mesh boxes. Indeed, the consistent way of indexing these points would have been through the use of “1/2”. For example, x_i would have been $x_{i+1/2}$ if the same indexing scheme as for the mesh boxes were used.

Nonetheless, the integer indexing scheme has some advantages in terms of computer

representation of the arrays x_i , y_j , and z_k . With the current indexing scheme, x_i corresponds to the right limit of x mesh i . Analogous relations hold true for the y and z directions.

The mesh-centred finite-difference discretization method approximates the average flux in mesh (i, j, k) , $\Phi_{i,j,k}$, by its value at the centre of the box:

$$\Phi_{i,j,k} = \Phi\left(\frac{x_i + x_{i-1}}{2}, \frac{y_j + y_{j-1}}{2}, \frac{z_k + z_{k-1}}{2}\right) \quad (33)$$

The average values of the flux on mesh boundaries are approximated by the flux values at the midpoints of the boundaries, denoted by $\Phi_{i\pm 1/2, j\pm 1/2, k\pm 1/2}$. For example,

$$\Phi_{i+1/2, j, k} = \Phi\left(x_i, \frac{y_j + y_{j-1}}{2}, \frac{z_k + z_{k-1}}{2}\right) \quad (34)$$

If the flux is discontinuous across a boundary, its average value on each side of the boundary can be indexed either with respect to the mesh to which it pertains or with respect to the boundary to which it refers. For example, the left value at the interface between mesh (i, j, k) and mesh $(i+1, j, k)$ can be denoted either by $\Phi_{i,j,k}^{x+}$ or by $\Phi_{i+1/2, j, k}^{x-}$. The first notation makes use of the fact that the value is to the right of the mesh (i, j, k) , whereas the second notation makes use of the fact that the value is to the left of the boundary $(i+1/2, j, k)$. The two notations will be used interchangeably. Similar notations will be used for derivatives and other quantities.

Assuming the medium to be homogeneous within every mesh box (i, j, k) , the two-group continuous diffusion equations for the (homogeneous) flux are written as in

Eq. (35)

$$\begin{aligned} -^1D \left(\frac{\partial^2(^1\Phi)}{\partial x^2} + \frac{\partial^2(^1\Phi)}{\partial y^2} + \frac{\partial^2(^1\Phi)}{\partial z^2} \right) + ^1\Sigma_r ^1\Phi &= \frac{1}{k_{eff}} \left(^1\nu\Sigma_f ^1\Phi + ^2\nu\Sigma_f ^2\Phi \right) \\ -^2D \left(\frac{\partial^2(^2\Phi)}{\partial x^2} + \frac{\partial^2(^2\Phi)}{\partial y^2} + \frac{\partial^2(^2\Phi)}{\partial z^2} \right) + ^2\Sigma_a ^2\Phi &= ^1\Sigma_s ^1\Phi \end{aligned} \quad (35)$$

where the left superscripts denote the energy group (i.e., energy group 1 or 2).

In what follows the finite differencing is illustrated for the x-direction and then results are extended to the y and z-direction. The group superscript is omitted, for clarity.

The backward-difference approximation of the left first derivative of the flux at the interface between nodes (i, j, k) and $(i + 1, j, k)$ is written as

$$\left(\frac{\partial \Phi}{\partial x} \right)_{i+1/2, j, k}^{x-} \approx \frac{\Phi_{i, j, k}^{x+} - \Phi_{i, j, k}}{h_{xi} / 2} \quad (36)$$

Similarly, the forward difference approximation to the right first derivative of the flux at the interface between nodes (i, j, k) and $(i + 1, j, k)$ is written as

$$\left(\frac{\partial \Phi}{\partial x} \right)_{i+1/2, j, k}^{x+} \approx \frac{\Phi_{i+1, j, k} - \Phi_{i+1, j, k}^{x-}}{h_{xi+1} / 2} \quad (37)$$

Note that in the above, the “+” and “-” signs are relative to the mesh for the fluxes and relative to the boundary for the derivatives.

The continuity of current and discontinuity of flux across boundaries can be used to express the boundary fluxes in terms of the center fluxes. First, the homogeneous-flux discontinuity across the mesh interface is applied.

$$f_{i,j,k}^{x+} \Phi_{i,j,k}^{x+} = f_{i+1,j,k}^{x-} \Phi_{i+1,j,k}^{x-} = \bar{\Psi}_{i+1/2,j,k} \quad (38)$$

It is to be noted that the heterogeneous flux, $\bar{\Psi}_{i+1/2,j,k}$, is continuous across the interface and hence it does not require references to its left and right values.

Combining Eq. (38) with Eqs. (36) and (37), the left and right derivatives at the interface can be expressed respectively as:

$$\left(\frac{\partial \Phi}{\partial x} \right)_{i+1/2,j}^- \approx \frac{\bar{\Psi}_{i+1/2,j,k} - \Phi_{i,j,k}}{h_{xi} / 2} \quad (39)$$

$$\left(\frac{\partial \Phi}{\partial x} \right)_{i+1/2,j,k}^+ \approx \frac{\Phi_{i+1,j,k} - \bar{\Psi}_{i+1/2,j,k}}{h_{xi+1} / 2} \quad (40)$$

The x-direction currents on the right and left of the interface are expressed as:

$$J_{i+1/2,j,k}^{x-} = -D_{i,j,k} \left(\frac{\partial \Phi}{\partial x} \right)_{i+1/2,j,k}^{x-} \quad (41)$$

$$J_{i+1/2,j,k}^{x+} = -D_{i+1,j,k} \left(\frac{\partial \Phi}{\partial x} \right)_{i+1/2,j,k}^{x+}$$

The continuity of current across the interface is thus written:

$$\left(\frac{2D_{i,j,k}}{h_{xi}}\right)\left(\frac{\bar{\Psi}_{i+1/2,j,k}}{f_{i,j,k}^{x+}} - \Phi_{i,j,k}\right) = \left(\frac{2D_{i+1,j,k}}{h_{xi+1}}\right)\left(\Phi_{i+1,j,k} - \frac{\bar{\Psi}_{i+1/2,j,k}}{f_{i+1,j,k}^{x-}}\right) \quad (42)$$

Solving for the interface heterogeneous flux in the above yields:

$$\bar{\Psi}_{i+1/2,j,k} = \frac{h_{xi+1}D_{i,j,k}\Phi_{i,j,k} + h_{xi}D_{i+1,j,k}\Phi_{i+1,j,k}}{\frac{h_{xi+1}D_{i,j,k}}{f_{i,j,k}^{x+}} + \frac{h_{xi}D_{i+1,j,k}}{f_{i+1,j,k}^{x-}}} \quad (43)$$

Substituting Eq. (43) into Eq. (40) yields the derivative for the right boundary of mesh

(i, j, k) :

$$\left(\frac{\partial\Phi}{\partial x}\right)_{i+1/2,j,k}^{x-} = \frac{2D_{i+1,j,k}(f_{i+1,j,k}^{x-}\Phi_{i+1,j,k} - f_{i,j,k}^{x+}\Phi_{i,j,k})}{f_{i+1,j,k}^{x-}h_{xi+1,j,k}D_{i,j,k} + f_{i,j,k}^{x+}h_{xi,j,k}D_{i+1,j,k}} \quad (44)$$

Following an argument similar to that for the right boundary, the derivative at the

left boundary of mesh (i, j, k) is:

$$\left(\frac{\partial\Phi}{\partial x}\right)_{i-1/2,j,k}^{x+} = \frac{2D_{i-1,j,k}(f_{i,j,k}^{x-}\Phi_{i,j,k} - f_{i-1,j,k}^{x+}\Phi_{i-1,j,k})}{f_{i,j,k}^{x-}h_{xi}D_{i-1,j,k} + f_{i-1,j,k}^{x+}h_{xi-1}D_{i,j,k}} \quad (45)$$

Equations (44) and (45) can now be used to approximate the second-order derivative

in x for mesh (i, j, k) :

$$\left(\frac{\partial^2\Phi}{\partial x^2}\right)_{i,j,k} = \frac{1}{h_{xi}} \left[\left(\frac{\partial\Phi}{\partial x}\right)_{i+1/2,j,k}^{x-} - \left(\frac{\partial\Phi}{\partial x}\right)_{i-1/2,j,k}^{x+} \right] = \frac{1}{h_{xi}} \left[\frac{2D_{i+1,j,k}(f_{i+1,j,k}^{x-}\Phi_{i+1,j,k} - f_{i,j,k}^{x+}\Phi_{i,j,k})}{f_{i+1,j,k}^{x-}h_{xi+1,j,k}D_{i,j,k} + f_{i,j,k}^{x+}h_{xi,j,k}D_{i+1,j,k}} - \frac{2D_{i-1,j,k}(f_{i,j,k}^{x-}\Phi_{i,j,k} - f_{i-1,j,k}^{x+}\Phi_{i-1,j,k})}{f_{i,j,k}^{x-}h_{xi}D_{i-1,j,k} + f_{i-1,j,k}^{x+}h_{xi-1}D_{i,j,k}} \right] \quad (46)$$

To simplify notation, some new quantities are introduced:

$$a_{i,j,k}^{x+} = \frac{-D_{i,j,k}}{h_{xi}} \frac{2f_{i+1,j,k}^{x-} D_{i+1,j,k}}{f_{i+1,j,k}^{x-} h_{xi+1} D_{i,j,k} + f_{i,j,k}^{x+} h_{xi} D_{i+1,j,k}} \quad (47)$$

$$a_{i,j,k}^{cx+} = \frac{-D_{i,j,k}}{h_{xi}} \frac{2f_{i,j,k}^{x+} D_{i+1,j,k}}{f_{i+1,j,k}^{x-} h_{xi+1} D_{i,j,k} + f_{i,j,k}^{x+} h_{xi} D_{i+1,j,k}} \quad (48)$$

$$a_{i,j,k}^{cx-} = \frac{-D_{i,j,k}}{h_{xi}} \frac{2f_{i,j,k}^{x-} D_{i-1,j,k}}{f_{i,j,k}^{x-} h_{xi} D_{i-1,j,k} + f_{i-1,j,k}^{x+} h_{xi-1} D_{i,j,k}} \quad (49)$$

$$a_{i,j,k}^{x-} = \frac{-D_{i,j,k}}{h_{xi}} \frac{2f_{i-1,j,k}^{x+} D_{i-1,j,k}}{f_{i,j,k}^{x-} h_{xi} D_{i-1,j,k} + f_{i-1,j,k}^{x+} h_{xi-1} D_{i,j,k}} \quad (50)$$

In terms of these new quantities, Eq. (46) is written as:

$$\left(\frac{\partial^2 \Phi}{\partial x^2} \right)_{i,j,k} = \frac{-1}{D_{i,j,k}} \left[a_{i,j,k}^{x+} \Phi_{i+1,j,k} - (a_{i,j,k}^{cx+} + a_{i,j,k}^{cx-}) \Phi_{i,j,k} + a_{i,j,k}^{x-} \Phi_{i-1,j,k} \right] \quad (51)$$

The superscripts on the above coefficients indicate to which boundary of the mesh they refer. Coefficients that multiply the current (central) mesh flux, (i, j, k) , have a “c” superscript. Coefficients that multiply fluxes in neighboring meshes do not have the “c” superscript.

Relations similar to Eq. (51) can be derived for the y and z-directions.

$$\left(\frac{\partial^2 \Phi}{\partial y^2} \right)_{i,j,k} = \frac{-1}{D_{i,j,k}} \left[a_{i,j,k}^{y+} \Phi_{i,j+1,k} - (a_{i,j,k}^{cy+} + a_{i,j,k}^{cy-}) \Phi_{i,j,k} + a_{i,j,k}^{y-} \Phi_{i,j-1,k} \right] \quad (52)$$

$$\left(\frac{\partial^2 \Phi}{\partial z^2} \right)_{i,j,k} = \frac{-1}{D_{i,j,k}} \left[a_{i,j,k}^{z+} \Phi_{i,j,k+1} - (a_{i,j,k}^{cz+} + a_{i,j,k}^{cz-}) \Phi_{i,j,k} + a_{i,j,k}^{z-} \Phi_{i,j,k-1} \right] \quad (53)$$

Applying the finite-difference approximation to the two-group diffusion equations

the following system of linear algebraic equations results:

$$\begin{aligned}
& {}^1a_{i,j,k}^{x+1} \Phi_{i+1,j,k} + {}^1a_{i,j,k}^{y+1} \Phi_{i,j+1,k} + {}^1a_{i,j,k}^{z+1} \Phi_{i,j,k+1} \\
& - \left({}^1a_{i,j,k}^{cx+} + {}^1a_{i,j,k}^{cy+} + {}^1a_{i,j,k}^{cz+} + {}^1a_{i,j,k}^{cx-} + {}^1a_{i,j,k}^{cy-} + {}^1a_{i,j,k}^{cz-} \right) \Phi_{i,j,k} \\
& + {}^1a_{i,j,k}^{x-1} \Phi_{i-1,j,k} + {}^1a_{i,j,k}^{y-1} \Phi_{i,j-1,k} + {}^1a_{i,j,k}^{z-1} \Phi_{i,j,k-1} + \Sigma_{r1} \Phi_{i,j,k} \\
& = \frac{1}{k_{eff}} \left(\nu \Sigma_{f1} \Phi_{i,j,k} + \nu \Sigma_{f2} \Phi_{i,j,k} \right) \\
& {}^2a_{i,j,k}^{x+2} \Phi_{i+1,j,k} + {}^2a_{i,j,k}^{y+2} \Phi_{i,j+1,k} + {}^2a_{i,j,k}^{z+2} \Phi_{i,j,k+1} \\
& - \left({}^2a_{i,j,k}^{cx+} + {}^2a_{i,j,k}^{cy+} + {}^2a_{i,j,k}^{cz+} + {}^2a_{i,j,k}^{cx-} + {}^2a_{i,j,k}^{cy-} + {}^2a_{i,j,k}^{cz-} \right) \Phi_{i,j,k} \\
& + {}^2a_{i,j,k}^{x-2} \Phi_{i-1,j,k} + {}^2a_{i,j,k}^{y-2} \Phi_{i,j-1,k} + {}^2a_{i,j,k}^{z-2} \Phi_{i,j,k-1} + \Sigma_{a2} \Phi_{i,j,k} \\
& = \Sigma_{12} \Phi_{i,j,k}
\end{aligned} \tag{54}$$

The following additional new quantities

$$\begin{aligned}
{}^1a_{i,j,k}^c &= - \left({}^1a_{i,j,k}^{cx+} + {}^1a_{i,j,k}^{cy+} + {}^1a_{i,j,k}^{cz+} + {}^1a_{i,j,k}^{cx-} + {}^1a_{i,j,k}^{cy-} + {}^1a_{i,j,k}^{cz-} \right) + \Sigma_{r1} \\
{}^2a_{i,j,k}^c &= - \left({}^2a_{i,j,k}^{cx+} + {}^2a_{i,j,k}^{cy+} + {}^2a_{i,j,k}^{cz+} + {}^2a_{i,j,k}^{cx-} + {}^2a_{i,j,k}^{cy-} + {}^2a_{i,j,k}^{cz-} \right) + \Sigma_{a2}
\end{aligned} \tag{55}$$

simplify the linear system to

$$\begin{aligned}
& {}^1a_{i,j,k}^{x+1} \Phi_{i+1,j,k} + {}^1a_{i,j,k}^{y+1} \Phi_{i,j+1,k} + {}^1a_{i,j,k}^{z+1} \Phi_{i,j,k+1} \\
& + {}^1a_{i,j,k}^{x-1} \Phi_{i-1,j,k} + {}^1a_{i,j,k}^{y-1} \Phi_{i,j-1,k} + {}^1a_{i,j,k}^{z-1} \Phi_{i,j,k-1} + {}^1a_{i,j,k}^c \Phi_{i,j,k} \\
& = \frac{1}{k_{eff}} \left(\nu \Sigma_{f1} \Phi_{i,j,k} + \nu \Sigma_{f2} \Phi_{i,j,k} \right) \\
& {}^2a_{i,j,k}^{x+2} \Phi_{i+1,j,k} + {}^2a_{i,j,k}^{y+2} \Phi_{i,j+1,k} + {}^2a_{i,j,k}^{z+2} \Phi_{i,j,k+1} \\
& + {}^2a_{i,j,k}^{x-2} \Phi_{i-1,j,k} + {}^2a_{i,j,k}^{y-2} \Phi_{i,j-1,k} + {}^2a_{i,j,k}^{z-2} \Phi_{i,j,k-1} + {}^2a_{i,j,k}^c \Phi_{i,j,k} \\
& = \Sigma_{12} \Phi_{i,j,k}
\end{aligned} \tag{56}$$

The linear systems derived above apply to interior meshes. For boundary meshes,

different expressions for the coefficients must be derived. The derivation will be

presented only for the boundary perpendicular to the x-axis and then extended to the y and z-directions.

The formalism is developed for homogeneous boundary conditions. To allow boundary conditions as general as possible to be simulated, mixed homogeneous boundary conditions are implemented by imposing the outward-current-to-flux ratio on each boundary

$$\gamma_{boundary} = \left(\frac{\vec{J}\hat{n}}{\Psi} \right)_{boundary} \quad (57)$$

where \hat{n} is the unit normal to the outer boundary of the domain.

Mixed homogeneous boundary conditions allow great flexibility in simulating different boundary conditions. Through the choice of γ , reflective, zero-flux, and vacuum boundary conditions can all be simulated. Vacuum boundary conditions can be transport-corrected or not. Additionally, artificial boundary conditions can be imposed at the limit of the fuel region, to simulate the presence of the reflector without actually modelling reflector meshes.

For an x-boundary node (b, j, k) , the outward-current-to-flux ratio becomes

$$\gamma^{xu} = \frac{u\bar{J}_{b+u/2,j,k}^x}{\bar{\Psi}_{b+u/2,j,k}} = \frac{u\bar{J}_{b,j,k}^{xu}}{f_{b,j,k}^{xu} \Phi_{b,j,k}^{xu}} = \frac{u\bar{J}_{b+u/2,j,k}^{x(-u)}}{f_{b,j,k}^{xu} \Phi_{b,j,k}^{xu}} \quad (58)$$

In the above, “ u ” is the sign of the outward unit normal to the external boundary. It is -1 for the left boundary and +1 for the right boundary.

By applying the finite-differencing techniques to the boundary node, the derivative on the boundary is written as:

$$\left(\frac{\partial\Phi}{\partial x}\right)_{b+u/2,j,k}^{x(-u)} = u \frac{\Phi_{b,j,k}^{xu} - \Phi_{b,j,k}}{\frac{h_{xb}}{2}} \quad (59)$$

The boundary current is written as:

$$J_{b,j,k}^{x(-u)} = u \frac{-D_{b,j,k} \left(\Phi_{b,j,k}^{xu} - \Phi_{b,j,k} \right)}{\frac{h_{xb}}{2}} \quad (60)$$

The boundary condition becomes:

$$\gamma^{xu} = \frac{-D_{b,j,k} \left(\Phi_{b,j,k}^{xu} - \Phi_{b,j,k} \right)}{\frac{h_{xb}}{2} f_{b,j,k}^{xu} \Phi_{b,j,k}^{xu}} \quad (61)$$

The boundary homogeneous flux is written:

$$\Phi_{b,j,k}^{x-} = \frac{2D_{b,j,k} \Phi_{b,j,k}}{h_{xb} \gamma^{x-} f_{b,j,k}^{x-} + 2D_{b,j,k}} \quad (62)$$

By substituting Eq. (62) into (59), the first derivative of the flux for the boundary becomes

$$\left(\frac{\partial\Phi}{\partial x}\right)_{b+u/2,j,k}^{xu} = \frac{\Phi_{b,j,k}}{\frac{D_{b,j,k}}{\gamma^{xu} f_{b,j,k}^{xu}} + \frac{h_{xb}}{2}} = \frac{-h_{xb}}{D_{b,j,k}} a_{b,j,k}^{cxu} \Phi_{b,j,k} \quad (63)$$

where $a_{b,j,k}^{cxu}$ is defined as

$$a_{b,j,k}^{cxu} = \frac{-1}{h_{xb} \left(\frac{1}{\gamma^{xu} f_{b,j,k}^{xu}} + \frac{h_{xb}}{2D_{b,j,k}} \right)} \quad (64)$$

The second partial derivative in x for a boundary mesh can now be expressed as:

$$\left(\frac{\partial^2\Phi}{\partial x^2}\right)_{b,j,k} = -\frac{1}{D_{b,j,k}} \left[a_{b-u,j,k}^{x(-u)} \Phi_{b-u,j,k} - \left(a_{b,j,k}^{cx(-u)} + a_{b,j,k}^{cxu} \right) \Phi_{b,j,k} \right] \quad (65)$$

Equation (65) is the counterpart of Eq. (51) for boundary meshes. The differences reside in the absence of coefficient $a_{b,j,k}^{xu}$ and in the different expression for coefficient $a_{b,j,k}^{cxu}$. Coefficients $a_{b-u,j,k}^{x(-u)}$ and $a_{b,j,k}^{cx(-u)}$ are identical to those in Eq. (51).

Arguments similar to Eq. (51) and (65) apply for the y and z-directions. The system remains valid, with the mention that some coefficients need to be modified for boundary meshes. Overall, six boundary conditions need to be provided to the code:

$(\gamma^{x-}, \gamma^{x+}, \gamma^{y-}, \gamma^{y+}, \gamma^{z-}, \text{ and } \gamma^{z+})$.

Using a node-size of one fuel lattice has been found to be sufficient for CANDU reactors.

Using a finer node size, which intuitively could provide a more accurate solution, has been found to produce less accurate results when fuel lattice homogenized cross

sections are used to solve the diffusion equation. This is unlike the situation for Light-Water Reactors (LWRs) which tend to see an improvement when using a finer node size (Shen, 2012b). This was determined to be mainly due to the fact that the fuel pins in a LWR are evenly distributed, unlike in CANDU which contains “clumped” fuel clusters separated by coolant and moderator. Using a mesh size smaller than a lattice cell for lattice-homogenized cross sections in a CANDU is not physically meaningful, as not all nodes will contain an even distribution of fuel in that case.

5.3 Global-Local Iterative Process

The first iteration cross sections for each heterogeneous node are calculated by DRAGON using a reflective boundary condition (RBC) assumption on each boundary. For reflective boundary conditions, the incoming current is equal to the outgoing current, and thus the albedos equal one.

$$\alpha_g^0 = 1 \tag{66}$$

The superscript “0” in the term denotes the fact that this albedo is for reflective, or zero current, boundary conditions.

Each material in the node has cross sections assigned from pre-generated DRAGON calculations which are collapsed into two neutron energy groups. Although DRAGON can perform calculations in many energy groups (69, 172, etc., depending on the microscopic cross section library), this work uses two energy groups for the transport calculation; the same number of groups used for the homogenized material cross

sections and full-core diffusion calculations. This is done to isolate the effect of spatial homogenization from that of group condensation. After solving for the flux distribution using the assumption of RBC in DRAGON, the node-homogenized parameters for the node are updated. The new node-averaged cross sections are found by performing a flux-weighted volume average calculation over the node as follows:

$$\hat{\Sigma}_g = \frac{\int \Sigma_g(\vec{r}) \Psi_g(\vec{r}) d^3\vec{r}}{\int \Psi_g(\vec{r}) d^3\vec{r}} \quad (67)$$

Once the neutronic parameters for each node are available, a full-core diffusion calculation is performed. For the full-core calculation, all nodes are assembled together. The neutron flux and current at the interface of each node with its neighbouring nodes are extracted from the results of the full-core calculation. This information is subsequently used to calculate node boundary conditions to be used for the single-node heterogeneous transport calculations in the next iteration step. It should be noted that the flux distribution obtained from the full-core calculation is the homogeneous flux. This is due to the fact that homogenized node parameters have been used and hence the neutronic parameters of individual regions in the node have been lost; replaced instead by a single set of values representing the entire homogenized node. Also noteworthy is the fact that, for the first iteration, the node-homogenized parameters are identical to those that would be obtained using SH. This is due to RBCs being used on the heterogeneous-node boundaries in the single-node transport calculations.

The next step in the process is to start a new iteration, by performing a new set of single-node transport calculations, one for each heterogeneous node. This is similar to the set of single-node heterogeneous calculations performed in the first iteration.

However, for the second and subsequent iterations, RBCs are not assumed. Instead, the node boundary conditions determined using the information obtained from the whole core calculation are used. The flux and current values extracted for each node boundary are used to calculate the current-to-flux ratio for that boundary:

$$\gamma_g = \frac{J_g}{\Phi_g} \quad (68)$$

This mechanism allows a reasonable correction for the actual leakage of each node, thus improving results in regions with high leakage such as close to the reflector or in the vicinity of strong absorbers where the high flux gradient in the core introduces challenges to the RBC assumption.

The new set of node boundary conditions are used to perform new heterogeneous-node calculations and generate a new set of cross sections and discontinuity factors to be used in a new full-core calculation. The iterative process is continued until convergence.

Figure 5 below shows the calculation process as a flow diagram.

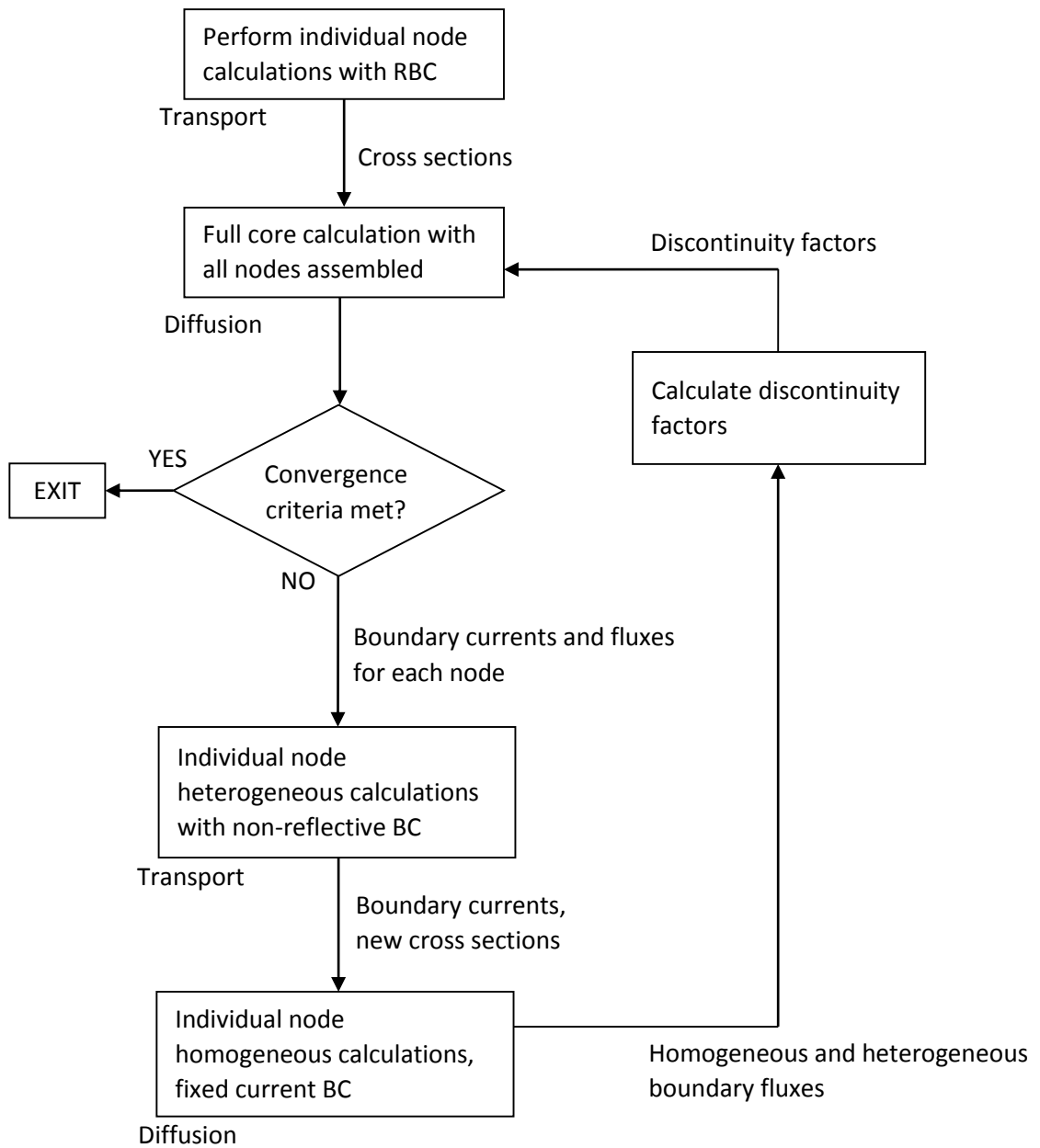


Figure 5 - Flow Chart of Iterative Calculation Process.

5.4 Node-Boundary Flux and Current from Full-Core Diffusion Calculation

The flux and current values on the boundaries of each node must be extracted from the full core diffusion calculation for use in the heterogeneous flux calculations for each node. The following equation is used to calculate the boundary flux between two nodes (i.e., the node interface flux):

$$\Phi^{interface} = \frac{\frac{D^- \Phi^-}{h_x^-} + \frac{D^+ \Phi^+}{h_x^+}}{\frac{D^-}{h_x^- f^-} + \frac{D^+}{h_x^+ f^+}} \quad (69)$$

where:

D represents the diffusion coefficient,

h_x represents the width of the mesh, and

f represents the discontinuity factor.

The subscripts for group number have been omitted for clarity, as the equation is identical for both groups. The “-” and “+” superscripts denote values for the left node and right node, respectively. Equation (69) essentially determines the continuous (heterogeneous) flux value at the node interface from the discontinuous (homogeneous) flux on each side of the boundary and the corresponding discontinuity factors.

The boundary current between two nodes is calculated as follows:

$$J = \frac{D^+ \left(\Phi^+ - \frac{\Phi^{interface}}{f^+} \right)}{\frac{h_x^+}{2}} \quad (70)$$

Using these equations, node interface fluxes and currents can be determined and used to calculate the current-to-flux ratio homogeneous boundary condition for each individual node.

5.5 Calculation of Discontinuity Factors

Once the leakage-corrected boundary conditions are applied to each node, heterogeneous calculations are performed in DRAGON. The boundary conditions from the diffusion calculations are initially extracted as the ratio of current to flux at the node boundary, represented by γ as defined in Eq. (68). As stated previously, boundary conditions in DRAGON are input as albedos, which are calculated as the ratio of incoming to outgoing current at the boundary. A conversion must therefore be done from boundary-condition γ to boundary-condition α in order to perform heterogeneous node calculations in DRAGON. The conversion is derived as follows (group subscripts have been omitted for clarity):

The net current is the difference between the incoming and outgoing currents:

$$J = J^{in} - J^{out} \quad (71)$$

The net current can also be approximated using Fick's Law:

$$J = -D \frac{d\Phi}{dx} \quad (72)$$

In the diffusion approximation, the incoming current can be expressed as (Ott and Bezella, 1989):

$$J^{out} = \frac{1}{4}\Phi + \frac{1}{2}D \frac{d\Phi}{dx} = \frac{1}{4}\Phi - \frac{1}{2}J \quad (73)$$

Similarly, the outgoing current is approximated as:

$$J^{in} = \frac{1}{4}\Phi - \frac{1}{2}D \frac{d\Phi}{dx} = \frac{1}{4}\Phi + \frac{1}{2}J \quad (74)$$

Substituting these equations in the albedo definition yields:

$$\alpha = \frac{J^{out}}{J^{in}} = \frac{\frac{1}{4}\Phi - \frac{1}{2}J}{\frac{1}{4}\Phi + \frac{1}{2}J} \quad (75)$$

Simplifying the ratio in Eq. (75) by dividing all terms by $\Phi/4$ gives:

$$\alpha = \frac{1 - 2\frac{J}{\Phi}}{1 + 2\frac{J}{\Phi}} \quad (76)$$

which is written in terms of γ as defined in Eq. (68):

$$\alpha = \frac{1 - 2\gamma}{1 + 2\gamma} \quad (77)$$

The output from the heterogeneous node calculation with leakage-corrected boundary conditions is the heterogeneous flux and current at the node boundaries. Additionally, using the heterogeneous flux distribution, new flux-weighted volume average cross sections are calculated according to Eq. (67). To calculate the discontinuity factor, the homogeneous flux for each node must be calculated. To preserve the proper boundary condition on each node, fixed current boundary conditions are imposed on each

homogeneous node. The fixed current is calculated by multiplying the current-to-flux ratio (γ) from the full-core calculation with the heterogeneous boundary flux. The homogenized cross sections are taken from the updated cross sections as determined in the heterogeneous node calculation. The homogeneous flux at each boundary is then calculated for each individual node with homogenized properties. With this information, the discontinuity factor is calculated as the ratio of homogeneous to heterogeneous flux for each node.

6 Calculations and Results

6.1 Description of Code

The code created for implementing the iterative method was written in FORTRAN. It consists of a main program, named DF2G1D (Discontinuity Factor Leakage-Corrected 2 group 1 dimension), which calls all other subroutines. The program interfaces with the transport code DRAGON (version 306-LD) and the diffusion solver DISDIF3D (Nichita *et al*, 2007). Figure 6 illustrates the structure of subroutines for DF2G1D.

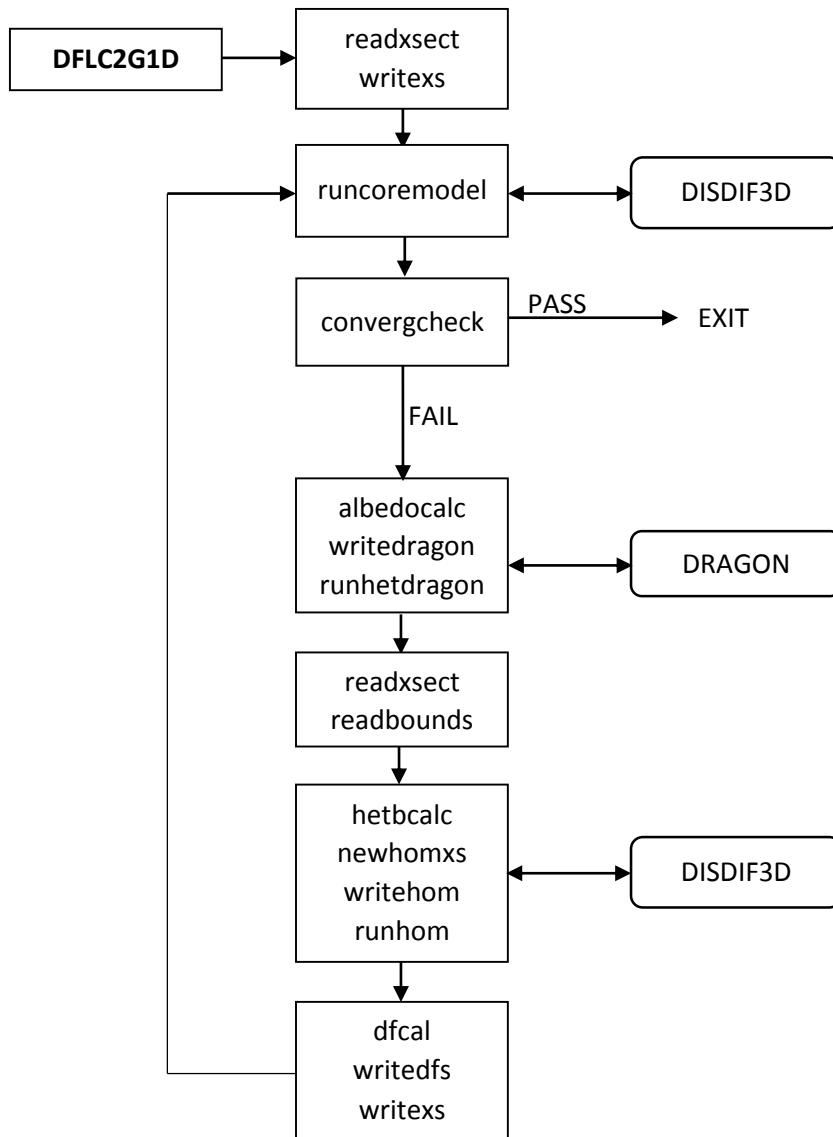


Figure 6 - Structure of Iterative Code DFLC2G1D.

The function of each subroutine is as follows:

- Readxsect, Writexs:** Read and write cross sections from DRAGON output files into diffusion code input files.
- Runcoremodel:** Runs a full core diffusion calculation by calling DISDIF3D.

Convercheck:	Calculates the percent difference in thermal and fast fluxes for each node between the current and the previous iteration. If the difference is less than 0.1%, iterations are stopped.
Albedocalc:	Uses the node interface flux and currents from the full core DISDIF3D calculation to calculate albedo boundary conditions.
Writedragon, Runhetdragon:	Writes new albedo values into DRAGON input files and runs DRAGON.
Readbounds:	Obtains the fast and thermal flux values on the boundary of each heterogeneous node from DRAGON output files.
Hetbcal:	Calculate current based on boundary flux output by DRAGON and gamma calculated from full core DISDIF3D output.
Newhomxs:	Divide fission cross sections by the heterogeneous node k-effective value for use in the fixed-current homogeneous node calculation.
Writehom, Runhom:	Writes and runs each homogeneous node input file for use with DISDIF3D.
Dfcal, Writedfs:	These subroutines calculate new discontinuity factors and write them into the DISDIF3D input file for use in the next iteration.

The program DFLC2G1D begins by extracting cross sections for each node previously calculated using reflective boundary conditions in DRAGON. These parameters are

passed to the diffusion code DISDIF3D which assembles all nodes together and performs a full core diffusion calculation. The fast flux, thermal flux, fast current, and thermal current at each node interface are extracted from the results of the diffusion calculation. These values allow the calculation of albedo boundary conditions using Eq. (77) for use in DRAGON. The albedos are input into DRAGON and the heterogeneous fluxes for each node are calculated. Leakage-corrected cross sections are extracted from the output of the DRAGON calculation as flux-weighted volume averages. The current on each heterogeneous node boundary is then calculated as the product of the boundary flux and gamma, as per Eq. (68). The homogeneous flux inside each node is determined by a single-node diffusion calculation using DISDIF3D with a fixed current boundary condition. Discontinuity factors for each node are calculated as the boundary heterogeneous flux divided by the boundary homogeneous flux. The new leakage-corrected cross sections and discontinuity factors are used in a new whole-core diffusion calculation, and the process iterates until both the thermal and fast flux in all nodes reach the convergence criteria of less than 0.1% change between consecutive global-local iterations.

6.2 Test Model

The iterative approach with discontinuity factors was implemented on a simplified one-dimensional PT-SCWR based model. Calculations were performed on five different core configurations using the iterative method and standard homogenization. Testing multiple different models allowed for a larger results data set, and an understanding of

how the accuracy of the suggested method varies with different core burnup characteristics.

The basic structure of the core model for all models under consideration consists of ten fuel nodes and one reflector node. The reflector node contains only moderator heavy water (acting as a neutron reflector in this case) and no fuel. The model of the core as represented in DRAGON is shown in Fig. 7.

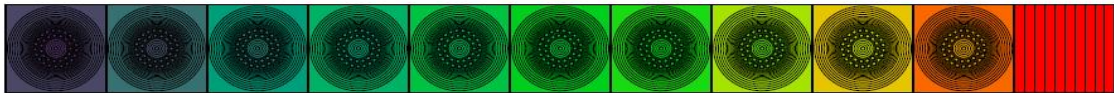


Figure 7 - PT-SCWR Based Core Model with 11 Nodes.

Utilizing an 11-node model saves significant computational time while taking advantage of fuel channel symmetry within a core. This configuration corresponds to a set of ten fuel nodes extending radially from the centre of the core outwards along with one reflector node, as depicted in Fig. 8 (Yetisir *et al*, 2011). This model provides an approximate representation of the radial power profile that is seen in the core when the neighbouring nodes are similar to those modelled here.

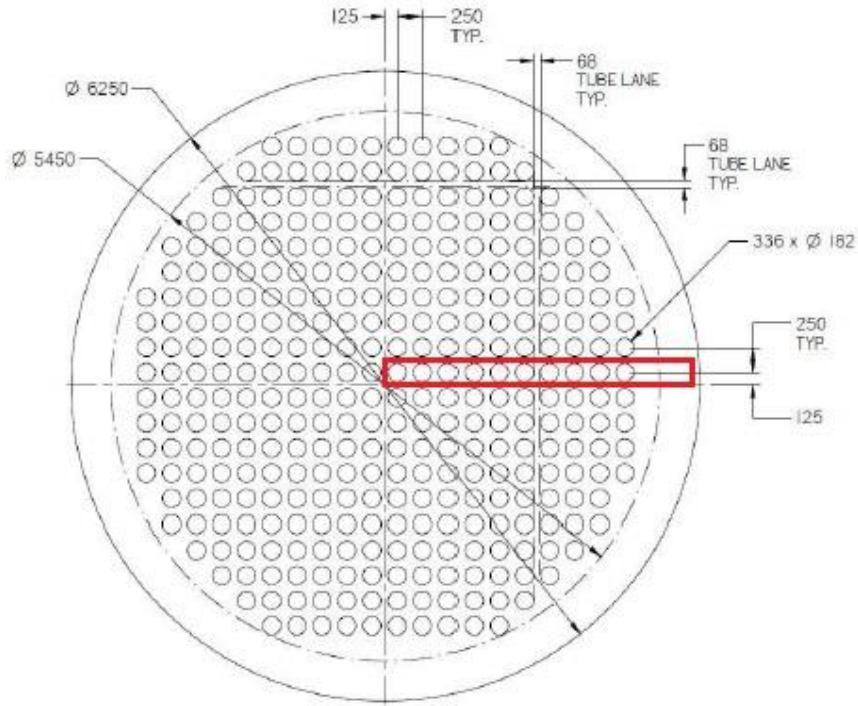


Figure 8 - Depiction of Test Model Nodes within PT-SCWR Core (Yetisir et al, 2011).

The five test cases under consideration have varying arrangements of irradiated and fresh fuel. This allows an insight on the impact that variations in burnup create. Burnup of the irradiated fuel was modelled as 40,000 kWd/kg, which is the anticipated discharge-burnup for the PT-SCWR fuel (McDonald, 2011).

The iterative calculation of discontinuity factors and boundary conditions was performed for the x-direction. The system boundary conditions for the y and z-directions are maintained as reflective for all iterations. The left system boundary condition is also reflective, while the right system boundary (after the reflector node) is a vacuum boundary. Neutrons are presumed to escape, but not re-enter, this node.

This condition corresponds to a physical boundary of the reactor core, where material outside of the reflector is more likely to absorb neutrons than to reflect them.

When applying iterated discontinuity factors to each node, calculation of discontinuity factors for the reflector node cannot be performed using the same type of transport calculation with homogeneous (current-to-flux ratio) boundary conditions employed for the fuel nodes because the reflector node lacks fission and hence an eigenvalue problem cannot be defined for it. Since the reflector node is homogeneous, a case can be made that, to the extent diffusion is a good approximation of transport, the discontinuity factor should equal exactly unity. Therefore, the decision was made to fix the discontinuity factors of the reflector node to unity.

6.2.1 Fuel Node Properties

Each fuel node has the same material and geometric representation in DRAGON.

Microscopic cross sections for 69-groups were used by DRAGON from the WIMSD4 library (Leszczynski *et al*, 2007), which varied depending on whether irradiated or new fuel was being modelled. The fuel represented is the 78 element second-generation Pu-Th PT-SCWR design (McDonald, 2011). Each fuel node is modelled with 78 fuel pins arranged in three concentric circles, with one large central pin composed of ZrO_2 . Figure 9 shows the geometrical model for one fuel node.

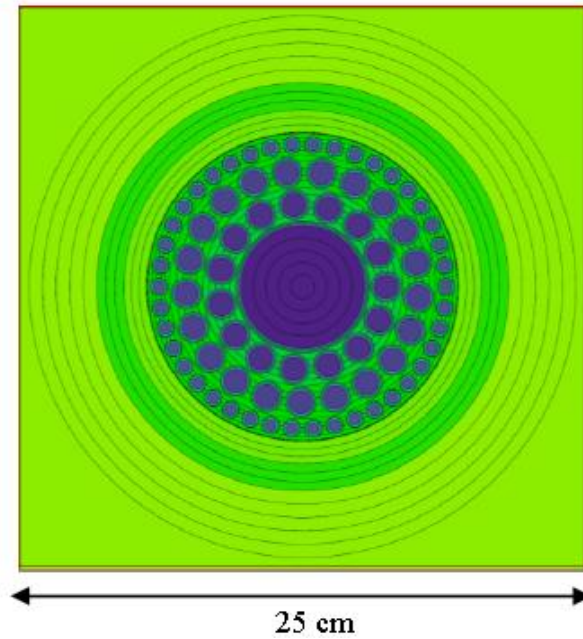


Figure 9 - Single fuel node model.

The sheath enclosing the fuel elements is composed of stainless steel. The fuel bundle is surrounded by the zirconium pressure tube, a stainless steel liner, a porous-zirconia insulator, and a calandria tube. Outside of this is the moderator region. Table 1 provides the properties used for each PT-SCWR fuel node.

Table 1 - Properties of Fuel Node in DRAGON

Moderator temperature	300 K
Moderator D ₂ O purity	99.833 at%
Lattice pitch	25 cm
Fuel pins in inner ring	15
Fuel pins in intermediate ring	21
Fuel pins in outer ring	42
Coolant	H ₂ O
Coolant Temperature	675 K
Fuel Material	Pu, Th, O
Fuel Temperature	900 K

In order to obtain the flux at the interface between fuel nodes, a very thin region was defined at each boundary of the fuel node. The reflector node also contains the same thin region on each boundary, onto which a neutron flux source is applied. This facilitates calculations on the reflector node, where there is no fuel and thus no neutron source. The source is calculated as the neutron leakage from the neighboring node on each particular boundary.

6.2.2 Configuration of Test Models

Results were produced for five different core configurations as follows:

- C1. 10 nodes with exit-burnup fuel and one reflector node;
- C2. 2 nodes with fresh fuel, 8 nodes exit-burnup fuel, and one reflector node;
- C3. 5 nodes fresh fuel, 5 nodes exit-burnup fuel, and one reflector node;
- C4. 8 nodes exit-burnup fuel, 2 nodes fresh fuel, and one reflector node; and
- C5. 10 nodes alternating between fresh and exit-burnup fuel, and one reflector node.

Configuration (1) contains the smallest burnup variation of the five models. All ten fuel nodes are identical, with cross sections corresponding to fuel at its anticipated exit burnup from the PT-SCWR. Since the neutron absorption and source across all nodes are the same, the flux profile of this case is anticipated to be smooth following roughly a cosine shape. Configuration (1) is thus the simplest test model of the five being tested.

A variation in burnup across the core is introduced in configuration (2), where the first two nodes contain fresh fuel and the remaining 8 correspond to exit-burnup fuel. The shift in burnup between the fresh and exit-burnup fuel is expected to cause a flux gradient at the interface between fuel types. This is similar to the arrangement in configuration (3), with the difference being that configuration (3) contains a larger number of fresh fuel nodes.

An abrupt change in burnup is introduced in configuration (4), where the fresh fuel nodes border the reflector node. In contrast to the relatively large fission cross section of the fresh fuel node, the reflector node has no fission source of its own, and a vacuum

boundary which contributes to neutron loss. A larger flux gradient will therefore be introduced here as compared to the previous test cases.

Configuration (5) contains the most varied fuel burnup distribution of all test cases. The fresh and exit-burnup fuel nodes are alternating, which results in a shift in neutronic properties between every node throughout the model. Due to the fact that a flux gradient will be present between each node, configuration (5) is the most complex of all the test models. This case corresponds to a bi-directional fuelling pattern, where fresh fuel is loaded from opposite ends of adjacent channels. This is the fuelling scheme currently used on CANDU reactors in operation. Although the PT-SCWR is not designed for online fuelling, configuration (5) is an interesting case nonetheless.

6.3 Comparison of Calculation Methods

The results of using leakage-corrected cross sections with discontinuity factors for the test models were compared with the results of four other calculation methods as shown below:

- M1. Full-core heterogeneous model (reference case);
- M2. Exact cross sections without discontinuity factors;
- M3. RBC cross sections with discontinuity factors;
- M4. RBC cross sections with no discontinuity factors; and
- M5. Iterated solution (leakage-corrected cross sections and discontinuity factors).

Method (1) is a calculation performed over the core which maintains the heterogeneous properties for each node. The flux is solved for with the neutron transport equation using DRAGON. Since the neutronic parameters for each node are never homogenized, no iterations or discontinuity factors are used. The flux solution obtained from this method is the heterogeneous flux. Producing these results is computationally demanding, which is why diffusion codes and homogenization methods are required for large-scale, full-core calculations. The heterogeneous flux and k-effective calculated from method (1) are the basis of comparison for all other methods. Method (1) is therefore referred to as the reference method.

In method (2), the boundary conditions for each node are extracted from the fluxes and currents calculated in the reference method. The cross sections that result from individual node heterogeneous calculations are therefore exact. However, no discontinuity factors are applied to the diffusion calculation. This allows a quantification of how discontinuity factors assist the calculation even when the benefit of exact cross-section information for each node is present. In reality, the results from the heterogeneous method would not be available and, therefore, method (2) could not be implemented. However, it is used here to explore the effect of the discontinuity factors.

The results obtained from assuming reflective boundary conditions and using discontinuity factors for each node is method (3). This is similar to method (2) without the benefit of having exact boundary conditions for each node. Instead, the assumption

of RBC is used when calculating new cross sections in the heterogeneous node calculation step. By comparing method (3) and method (2) with the reference, an understanding of how the RBC assumption effects the calculation results is provided.

In method (4), the homogenized neutron parameters are used without the benefit of discontinuity factors or leakage-corrected boundary conditions. This method is representative of the current standard for reactor physics calculations in CANDU reactors.

Method (5) represents the focus of this work, and consists of the iterated solution, which uses leakage-corrected cross sections and discontinuity factors.

6.4 Error Estimates

Characterizing the performance of the suggested method requires errors to be estimated. The parameters of interest in the case of reactor physics code outputs are generally node-averaged neutron flux values, fission rate density (indicative of the power density), and system eigenvalue (k_{eff}). The error in node-averaged thermal flux, fast flux, and fission rate density for each individual node are, therefore, evaluated for each calculation method.

The value of k_{eff} provides an indication of criticality. Since an online reactor will ideally operate close to criticality, any reactivity changes made by the program (e.g., fuelling, control rod movement) should strive to maintain the reactor critical. The error in the value of k_{eff} is also evaluated for result comparisons.

Using results from calculation method 1 (the heterogeneous results) as the reference, the root-mean square (RMS) error for the four other calculation methods was determined using Eq. 78:

$$RMS = \sqrt{\frac{\sum_{i=1}^n \left(\frac{y_i - y_{i-ref}}{y_{i-ref}} \right)^2}{n}} \quad (78)$$

6.5 Results

6.5.1 Configuration 1 (10 exit-burnup nodes)

Configuration 1 consists of ten nodes with exit-burnup fuel followed by an eleventh reflector node. Figures 10 to 12 show, respectively, plots of the node-average fast flux, node-average thermal flux, and node-average fission-rate density obtained using all calculation methods described in section 6.3. No fission rate density result is given for the eleventh, reflector, node, as no fuel and thus no fission is present in this node. For the iterated method, a total of 8 iterations were required to meet the convergence criterion of less than 0.1% change between consecutive iterations.

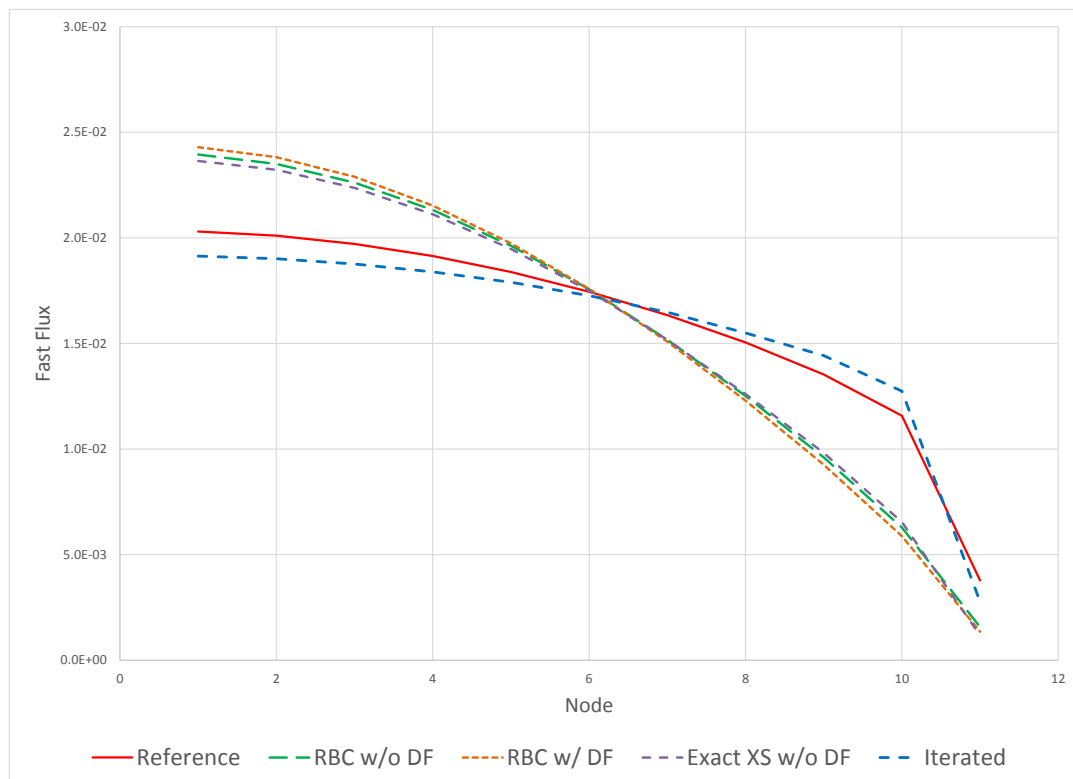


Figure 10 - Configuration 1 Fast Flux Results.

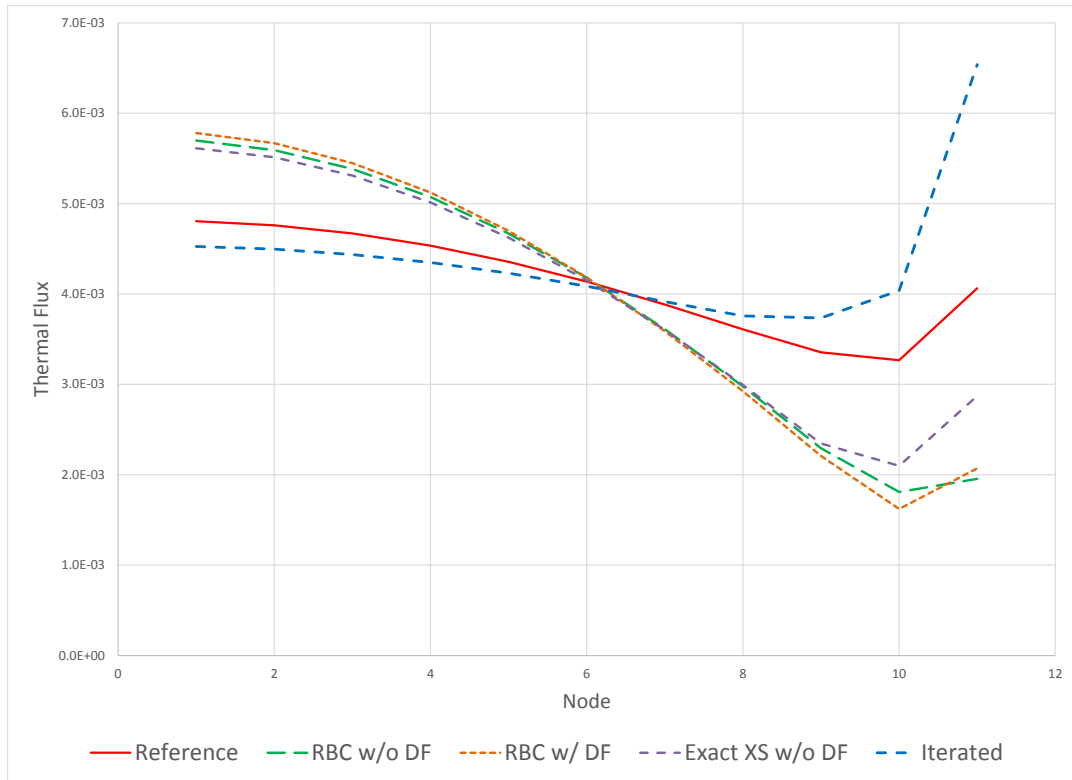


Figure 11 - Configuration 1 Thermal Flux Results.

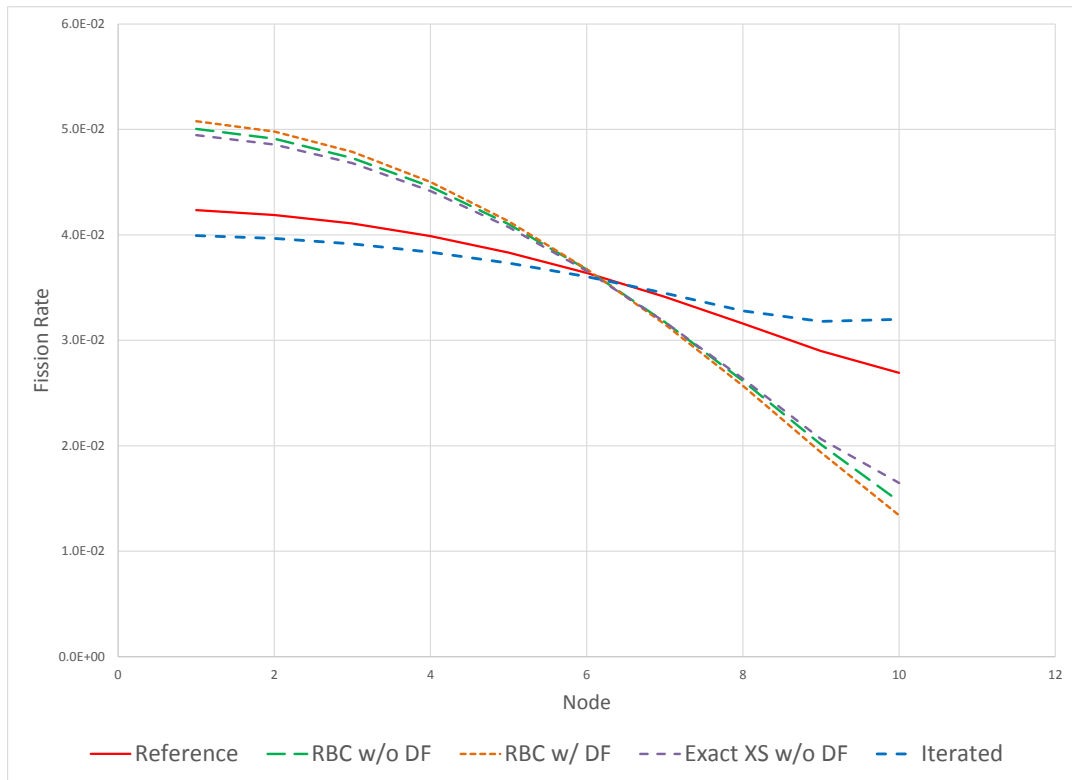


Figure 12 - Configuration 1 Fission Rate Results.

It can be seen that, for the uniform-burnup situation in configuration 1, the fast flux, thermal flux, and fission rate density in the fuel nodes decrease towards the side with the vacuum boundary condition. This is to be expected as neutrons leak out through that system boundary. The shape is similar to a discrete cosine which would be the shape of the solution for a homogeneous model treated in diffusion theory. A marked departure from a cosine shape occurs most clearly in the reflector node. The fast flux drops more abruptly in the reflector node because of the absence of a fast-neutron source in that node. Conversely, the thermal flux increases in the reflector node because of slowing down of fast neutrons streaming in from the last fuel node and because of the reduced thermal absorption in the absence of fuel. The large thermal flux in the reflector node causes thermal neutron leakage from the reflector to the neighbouring fuel node, which leads to a softening of the drop of that node's thermal flux and fission rate.

Table 2 summarizes the RMS errors for each calculation method used for configuration 1. It also provides the value of k-effective for each method, and the k-effective error in m_k , compared to the reference result.

Table 2 - Configuration 1 Errors

Method	K_{eff}	K_{eff} error (mk)	Fast Flux RMS% error	Thermal Flux RMS% error	Fission Rate RMS% error
Reference (M1)	0.88087	-	-	-	-
RBC w/o DF (M2)	0.88872	7.85	26.4	25.4	20.9
RBC w DF (M3)	0.88857	7.69	28.8	26.6	23.0
Exact XS w/o DF (M4)	0.88824	7.36	27.9	19.6	18.8
Iterative (M5)	0.88318	2.31	9.5	20.3	7.6

It can be seen that the iterated method provides the best accuracy, reducing the error in the effective multiplication constant, k_{eff} and the fission-rate density RMS to approximately one third of their respective values for the standard-homogenization method. The relatively modest reduction in the RMS for the thermal flux can be seen to be due, primarily, to a large error in the calculated thermal flux in the reflector. With the exception of the iterative method, all other methods overestimate the slope of the flux decrease.

6.5.2 Configuration 2 (2 fresh and 8 exit-burnup nodes)

Configuration 2 consists of two fresh fuel nodes, eight nodes of exit-burnup fuel, and an eleventh reflector node. Figures 13 to 15 show, respectively, plots of the node-average fast flux, node-average thermal flux, and node-average fission-rate density obtained using all calculation methods described in section 6.3. No fission rate density result is given for the eleventh, reflector, node, as no fuel and thus no fission is present in this node. For the iterated method, a total of 15 iterations were required to meet the convergence criterion of less than 0.1% change between consecutive iterations.

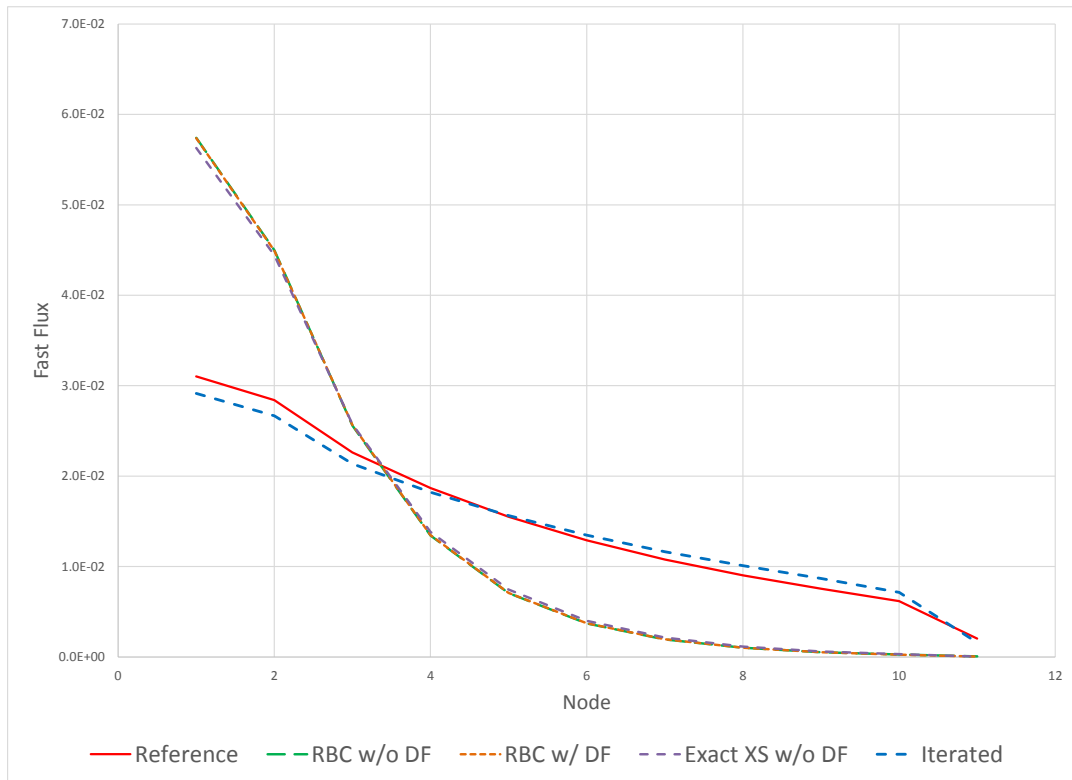


Figure 13 - Configuration 2 Fast Flux Results.

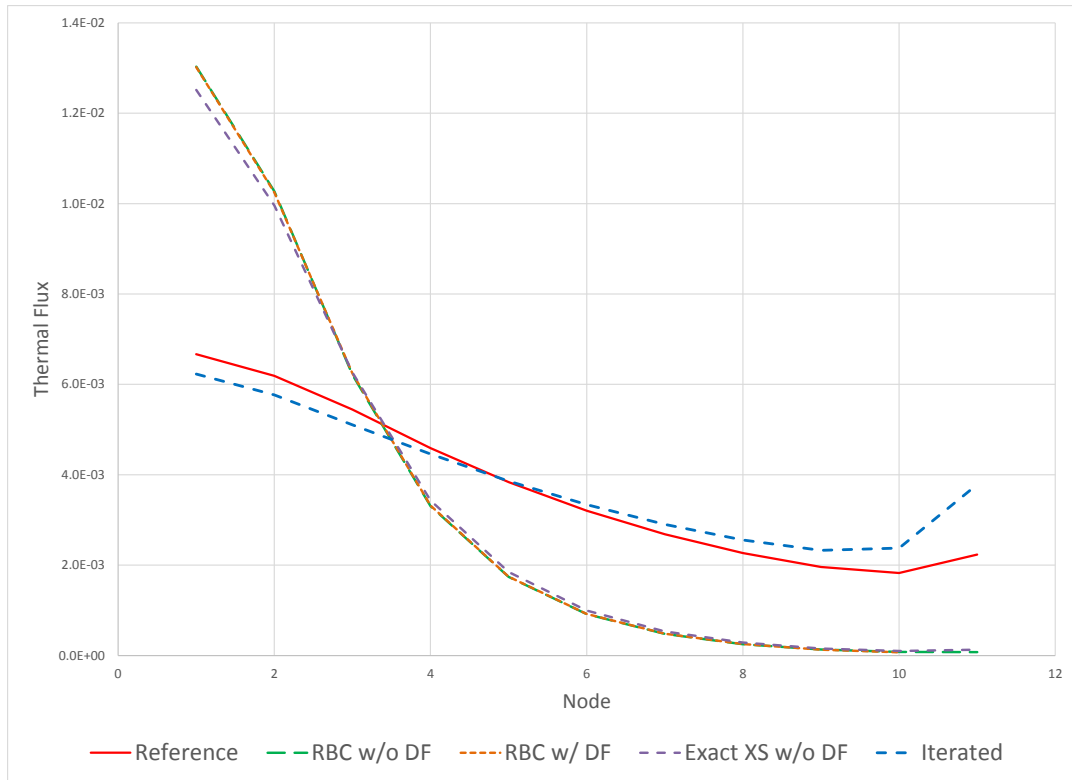


Figure 14 - Configuration 2 Thermal Flux Results.

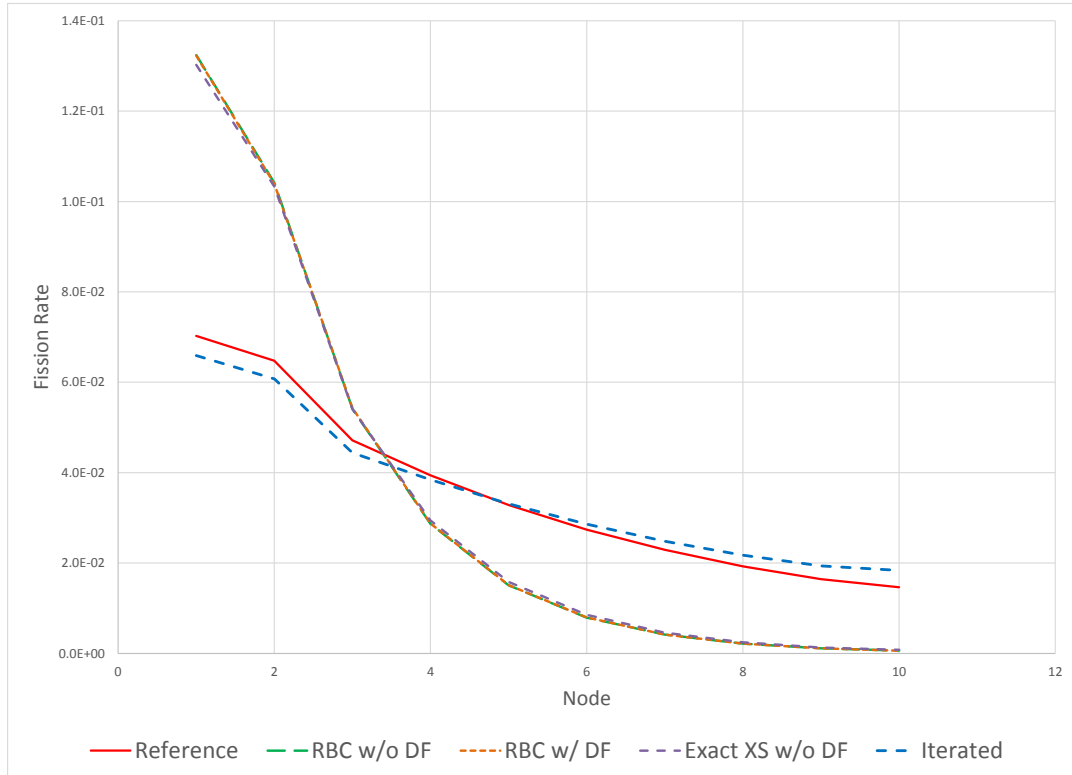


Figure 15 - Configuration 2 Fission Rate Results.

It can be seen that, for configuration 2, the fast flux, thermal flux, and fission rate density in the fuel nodes begin to drop precipitously after the second node due to the reduced fission cross section in fuel nodes 3 to 10 which have a high burnup. Similarity to a cosine shape is thus lost because of the burnup non-uniformity. Similarly to the situation in configuration 1, the fast flux drops more abruptly in the reflector node because of the absence of a fast-neutron source in that node. Conversely, the thermal flux increases in the reflector node because of slowing down of fast neutrons streaming in from the last fuel node and because of the reduced thermal absorption in the absence of fuel.

Table 3 summarizes the RMS errors for each calculation method used for configuration 2. This table also provides the value of k-effective for each method, and the k-effective error in mk as compared to the reference result.

Table 3 - Configuration 2 Errors

Method	K_{eff}	K_{eff} error (mk)	Fast Flux RMS% error	Thermal Flux RMS% error	Fission Rate RMS% error
Reference (M1)	0.93839	-	-	-	-
RBC w/o DF (M2)	0.99059	52.20	74.4	76.1	72.7
RBC w DF (M3)	0.99041	52.02	74.3	76.0	72.6
Exact XS w/o DF (M4)	0.98612	47.73	72.9	73.5	71.1
Iterative (M5)	0.93627	-2.11	10.9	24.3	11.6

As for configuration 1, it can be seen that the iterated method provides the best accuracy, reducing the fission-rate density RMS to approximately one sixth of its value for the standard-homogenization method. The improvement in the effective multiplication constant, k_{eff} , is even more impressive, as that error is reduced from 52 mk to 2 mk. As for configuration 1, all methods except for the one employing iterations show a steeper slope of decrease of fluxes and fission rate density.

6.5.3 Configuration 3 (5 fresh and 5 exit-burnup nodes)

Configuration 3 consists of five fresh fuel nodes, five nodes of exit-burnup fuel, and an eleventh reflector node. Figures 16 to 18 show, respectively, plots of the node-average fast flux, node-average thermal flux, and node-average fission-rate density obtained using all calculation methods described in section 6.3. No fission rate density result is given for the eleventh, reflector, node, as no fuel and thus no fission is present in this node. For the iterated method, a total of 15 iterations were required to meet the convergence criterion of less than 0.1% change between consecutive iterations.

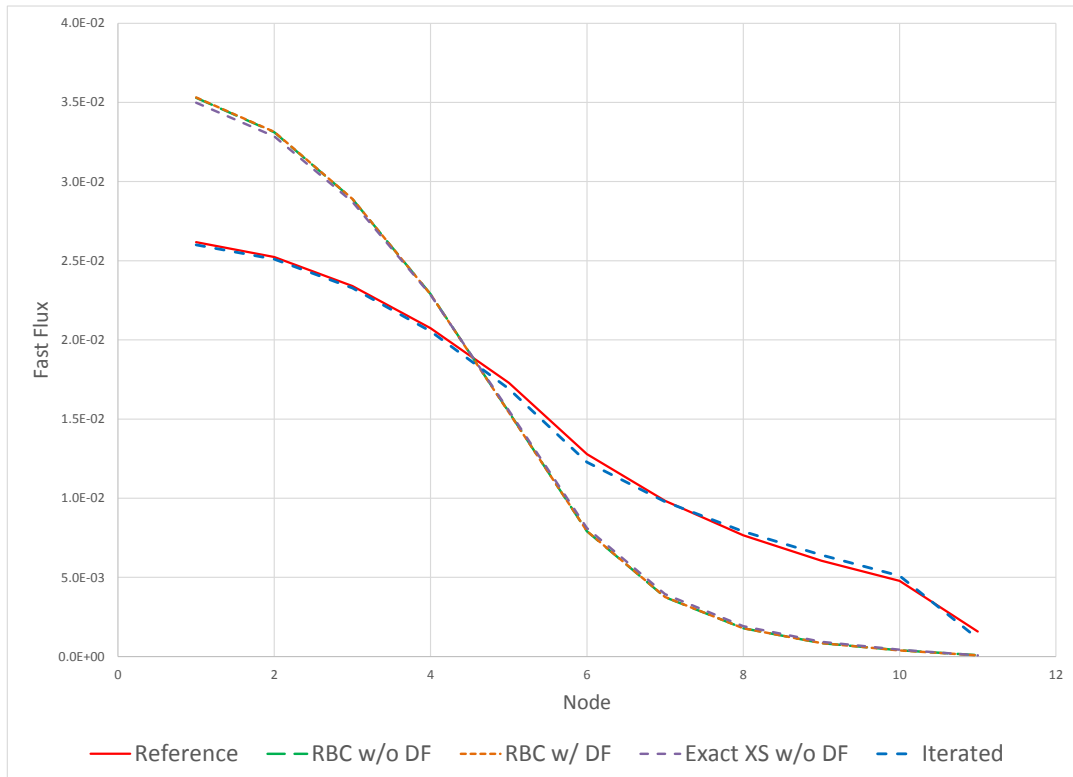


Figure 16 - Configuration 3 Fast Flux Results.

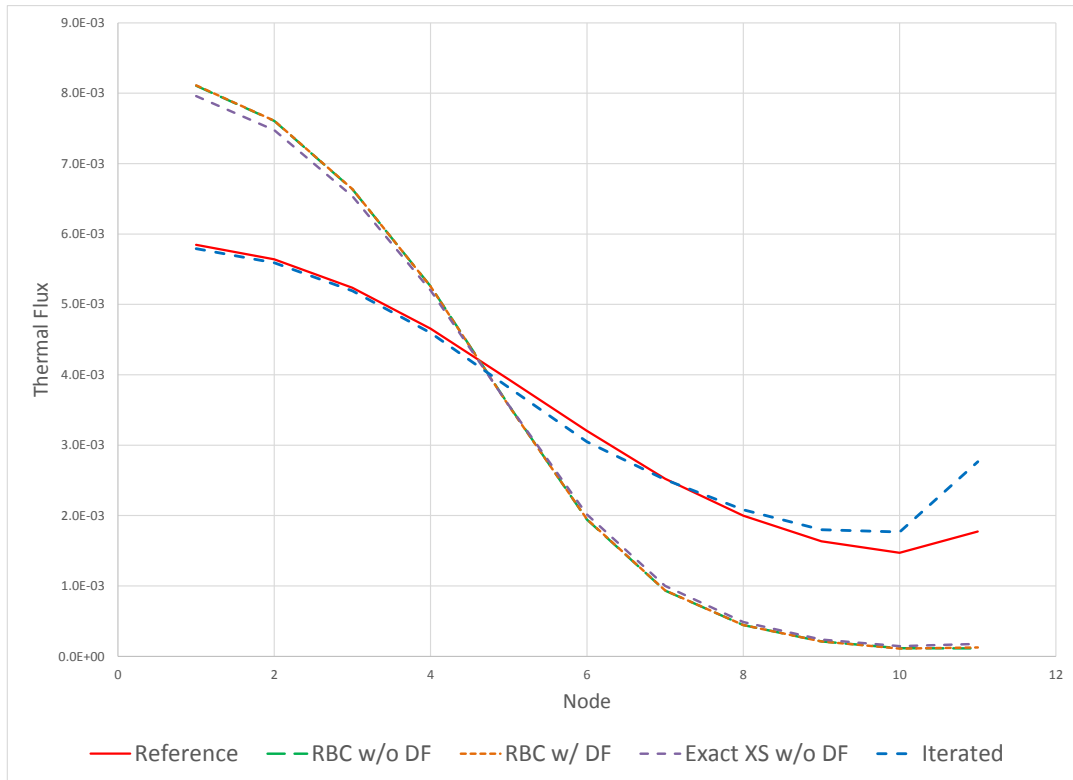


Figure 17 - Configuration 3 Thermal Flux Results.

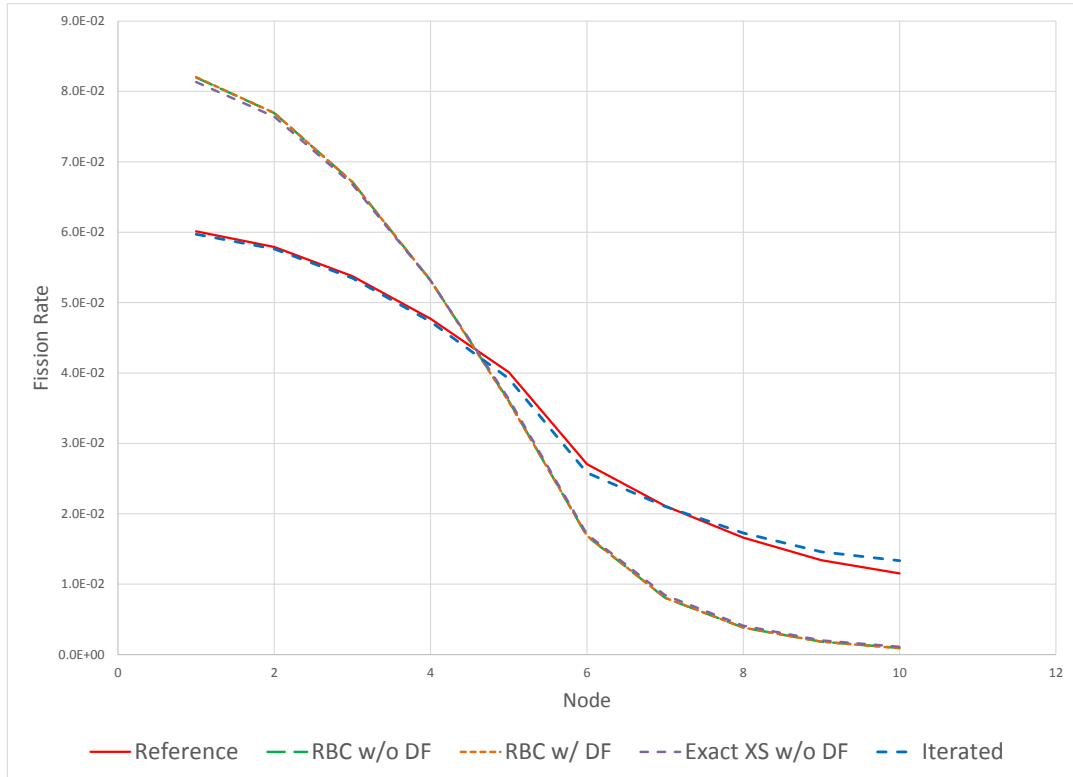


Figure 18 - Configuration 3 Fission Rate Results.

Table 4 summarizes the RMS errors for each calculation method used for configuration 3. This table also provides the value of k-effective for each method, and the k-effective error in mk as compared to the reference result.

Table 4 - Configuration 3 Errors

Method	K_{eff}	K_{eff} error (mk)	Fast Flux RMS% error	Thermal Flux RMS% error	Fission Rate RMS% error
Reference (M1)	0.99454	-	-	-	-
RBC w/o DF (M2)	1.02816	33.62	59.4	60.3	55.1
RBC w DF (M3)	1.02813	33.58	59.5	60.2	55.1
Exact XS w/o DF (M4)	1.02564	31.09	58.6	58.3	53.9
Iterative (M5)	0.99509	0.55	9.1	18.3	6.1

Results for configuration 3 are similar to those for configuration 2, with the only difference being that the steeper decrease in the flux and fission density occur at the new boundary between fresh and exit-burnup fuel, namely between nodes 4 and 5. Improvements in accuracy when using the iterated method compared to standard homogenization are similar to those seen in configuration 2.

6.5.4 Configuration 4 (8 exit-burnup and 2 fresh nodes)

Configuration 4 consists of eight exit-burnup fuel nodes, two nodes of fresh fuel, and an eleventh reflector node. Figures 19 to 21 show, respectively, plots of the node-average fast flux, node-average thermal flux, and node-average fission-rate density obtained using all calculation methods described in section 6.3. No fission rate density result is given for the eleventh, reflector, node, as no fuel and thus no fission is present in this node. For the iterated method, a total of 13 iterations were required to meet the convergence criterion of less than 0.1% change between consecutive iterations.

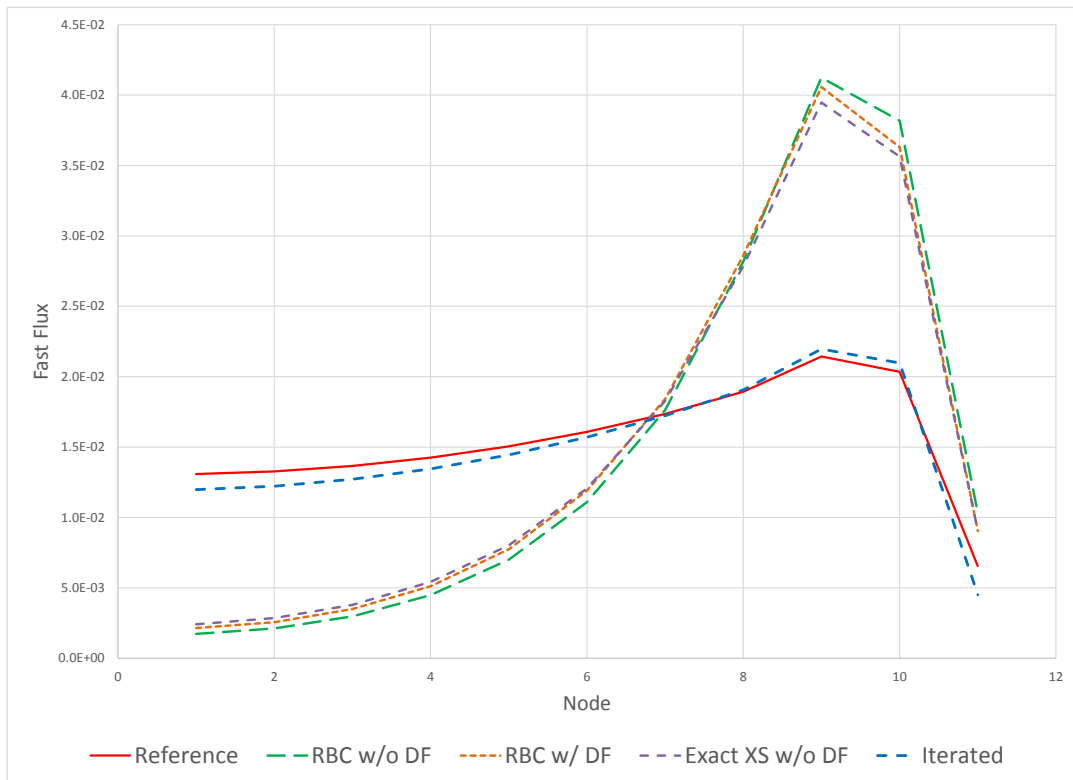


Figure 19 - Configuration 4 Fast Flux Results.

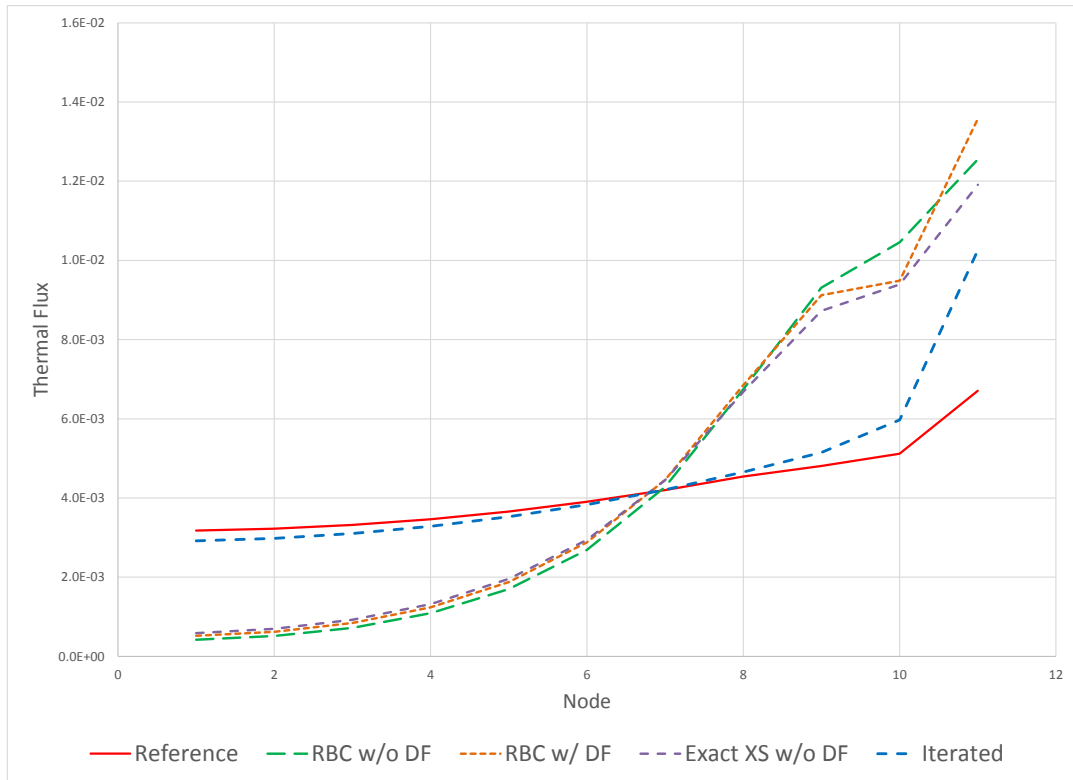


Figure 20 - Configuration 4 Thermal Flux Results.

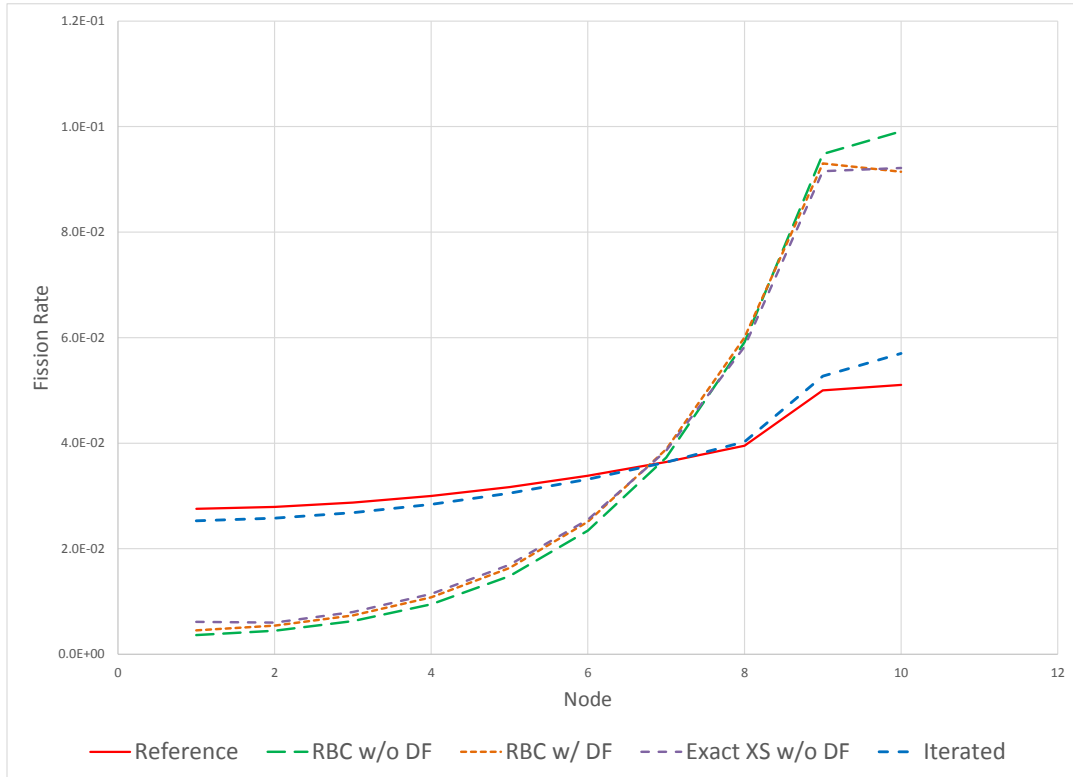


Figure 21 - Configuration 4 Fission Rate Results.

The main characteristic of configuration 4 is the presence of two fresh-fuel nodes close to the reflector. This causes the fast flux to increase towards the vacuum boundary up to node 9 and then drop abruptly in node 10 and the reflector node as the loss of neutrons through the boundary becomes prevalent. The thermal flux continues to increase in node 10 and the reflector node due to the slowing down of fast neutrons that stream to those nodes and the reduced thermal absorption in the reflector node in the absence of fuel material. The fission rate density increases up to node 9 and levels off in node 10 due to the proximity of the vacuum boundary.

Table 5 summarizes the RMS errors for each calculation method used for configuration 4. This table also provides the value of k-effective for each method, and the k-effective error in mk as compared to the reference result.

Table 5 - Configuration 4 Errors

Method	K_{eff}	K_{eff} error (mk)	Fast Flux RMS% error	Thermal Flux RMS% error	Fission Rate RMS% error
Reference (M1)	0.91082	-	-	-	-
RBC w/o DF (M2)	0.94233	31.50	68.3	73.3	69.6
RBC w DF (M3)	0.93655	25.73	63.6	70.7	65.2
Exact XS w/o DF (M4)	0.93331	22.48	61.2	65.1	63.0
Iterative (M5)	0.91955	8.72	10.5	17.5	6.2

For configuration 4, the iterated solution continues to be the most accurate, with a reduction in the k_{eff} error from 31 mk to 8 mk (approximately four fold) and almost a ten-fold reduction in the RMS for the fission rate. As in previous cases, non-iterated methods continue to overestimate the slope of the fluxes and fission rate density.

6.5.5 Configuration 5 (10 alternating fresh and exit-burnup nodes)

Configuration 5 consists of ten nodes alternating between fresh and exit-burnup fuel, and an eleventh reflector node. Figures 22 to 24 show, respectively, plots of the node-average fast flux, node-average thermal flux, and node-average fission-rate density obtained using all calculation methods described in section 6.3. No fission rate density result is given for the eleventh, reflector, node, as no fuel and thus no fission is present in this node. For the iterated method, a total of 15 iterations were required to meet the convergence criterion of less than 0.1% change between consecutive iterations.

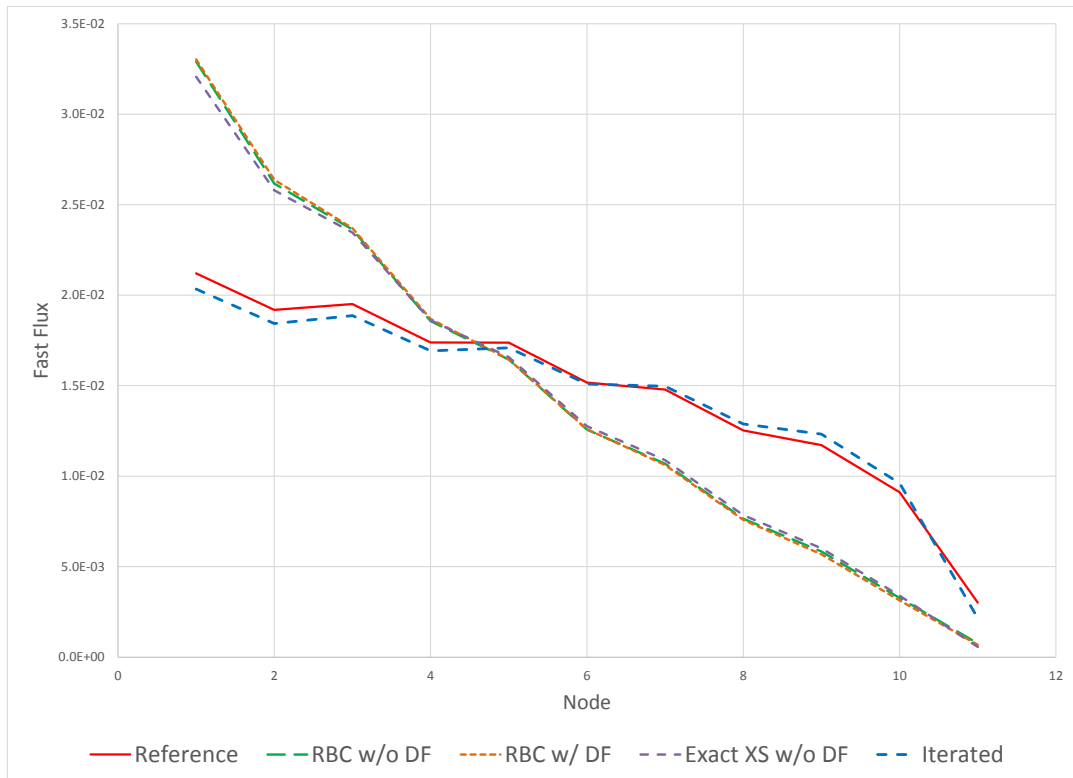


Figure 22 - Configuration 5 Fast Flux Results.

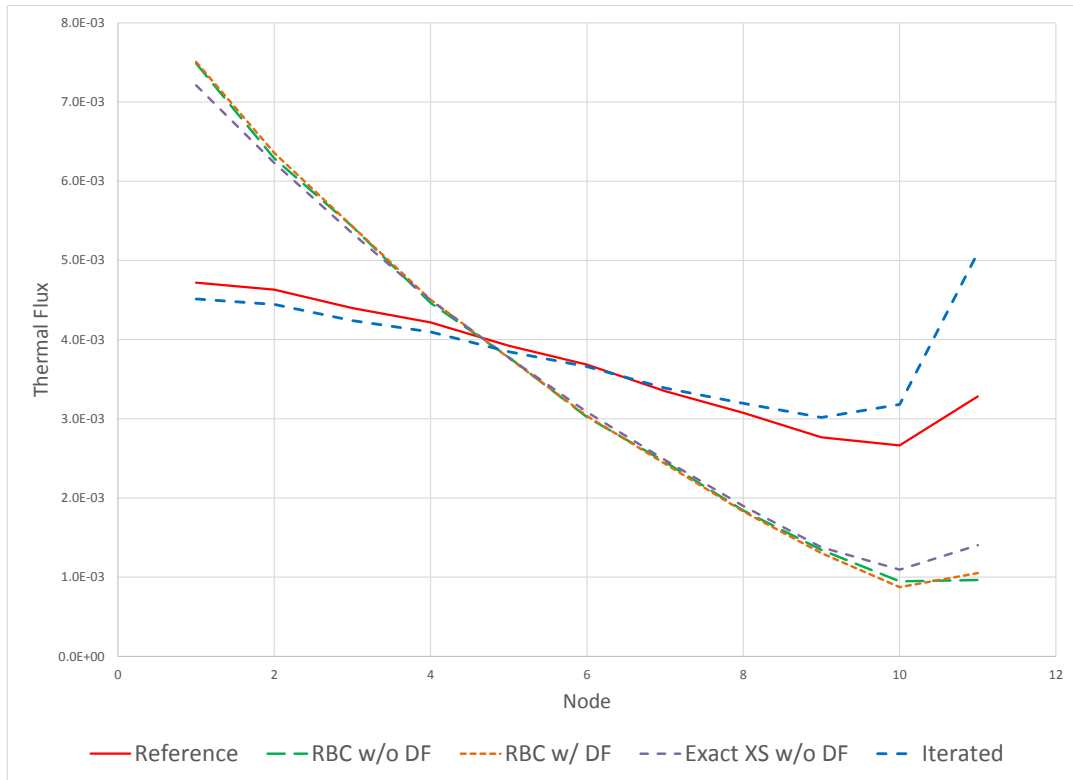


Figure 23 - Configuration 5 Thermal Flux Results.

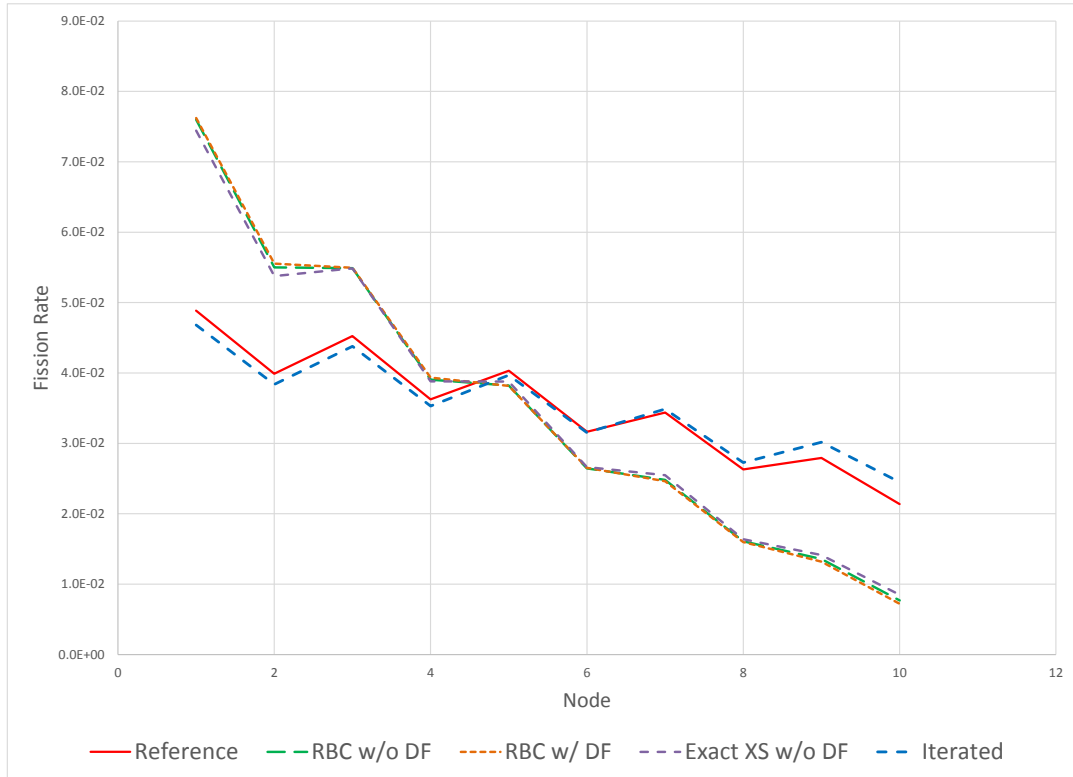


Figure 24 - Configuration 5 Fission Rate Results.

Results for configuration 5 are somewhat similar to those for configuration 1, in that there is an overall decrease in the flux and fission rate density going from the reflective boundary (left) to the vacuum boundary (right). Additionally, there is an overall undulation over-imposed on that shape due to the alternating fuel burnup. As in configuration 1, there is a sharper decrease in the fast flux in the reflector node due to the absence of a fission source and an increase in the thermal flux in the reflector due to slowing down of fast neutrons streaming into the reflector. Similar to the previous configurations, all non-iterative methods overestimate the flux and fission rate density slopes.

Table 6 summarizes the RMS errors for each calculation method used for configuration 5. This table also provides the value of k-effective for each method, and the k-effective error in mk as compared to the reference result.

Table 6 - Configuration 5 Errors

Method	K_{eff}	K_{eff} error (mk)	Fast Flux RMS% error	Thermal Flux RMS% error	Fission Rate RMS% error
Reference (M1)	0.96116	-	-	-	-
RBC w/o DF (M2)	0.97528	14.12	42.0	42.3	37.9
RBC w DF (M3)	0.97496	13.80	43.1	42.7	38.8
Exact XS w/o DF (M4)	0.97431	13.15	41.9	38.3	35.9
Iterative (M5)	0.96313	1.97	9.2	18.1	5.9

For configuration 5, the error in k_{eff} is reduced from 14 mk to 2 mk and the RMS for the fission rate density is reduced approximately six-fold, from 38% to 6%.

7 Discussion

The simple arrangement of nodes in configuration 1 shows that the iterated method results are very close to the fully heterogeneous reference case, particularly for the fast flux as shown in Fig. 10. The results for the thermal flux calculation in Fig. 11 show that the iterated method is slightly better than standard homogenization, and marginally worse than the calculation performed using standard homogenization with exact cross sections. It is to be noted, however, that the worst agreement for the iterated method occurs in the reflector, where discontinuity factors have been set to unity. However, the importance of the flux calculation in the reflector node is minimal, since there is no fission source and therefore no power is produced. The fission rate results for configuration 1 show that the iterated method results correspond well to those of the reference case, as seen in Fig. 12. The overall RMS percent error for the fission rate is about nine times lower for the iterated method than that of the standard homogenization methods, as seen in Table 2. This is significantly better than the iterated method RMS percent errors for fast and thermal flux, due to the fact that the reflector node does not have a fission source and therefore is not included in the fission rate results.

The results for configuration 2 show excellent correlation between the iterated method and the reference case, with a RMS percentage error of only 11% for the fast flux and 24% for the thermal flux as seen in Table 3. The RMS error was less for the iterated method as compared to any of the other calculations methods for the thermal flux. For

fast flux and fission rate calculations, the RMS error was significantly smaller for the iterated method than that of any other case. The value of k-effective was accurate to 10 mk for the iterated method, and to 100 mk for all other calculation methods.

Configuration 3 has a similar burnup shift through the core as configuration 2, with the difference being that the nodes are evenly split between fresh and exit-burnup fuel. The results of configuration 3 are similar to those of configuration 2. The RMS error for the iterated method is much less than the other cases for the thermal flux, and significantly less for the fast flux as shown in Table 4.

Configuration 4 has a more abrupt shift in burnup as compared to the first three configurations. In this configuration, the reflector node is neighbouring a fresh fuel node. The results for this configuration in Table 5 show that the iterated method has a RMS error much less than the other cases for the thermal flux, and significantly less for the fast flux. The system eigenvalue, k-effective, is accurate to 10 mk for the iterated method and 100 mk for all other calculation methods.

Configuration 5 is the most complex, due to shifts in burnup at the interface of each node. The results show that the iterated method corresponds very well with the heterogeneous reference case result. The RMS error for the iterated method is at least four times as small that of any other method for the fast flux, and at least twice as small

for the thermal flux as seen in Table 6. The RMS error for fission rate is about seven times smaller for the iterated method than for standard homogenization. The shape of the power profile as calculated by the iterated method is very close to the reference shape, which provides confidence that the iterated method can manage the constant shifts in burnup between nodes. The system eigenvalue is accurate to 10 mk for the iterated method and 100 mk for all other calculation methods.

Results for all configurations show that the fast flux tends to decrease towards the right side of the core model, where the reflector node is located. This is an expected result, as the reflector node does not have a fission source and thus cannot contribute to the creation of fast neutrons. The fast neutrons will either be down-scattered to the thermal neutron energy group, or be lost due to leakage out of the core. Conversely, the thermal flux tends to show an increase towards the reflector node for all configurations. This is due to the down-scattering of fast neutrons that occurs within the reflector node, increasing the population of thermal neutrons.

A survey of the five studied configurations reveals that for all of them, results obtained using non-iterated solutions tend to be grouped together and be quite far from the reference solution, whereas the iterated solution tends to be close to the reference one. This can be explained by the fact that homogenized cross sections have a strong dependence on burnup but a weak dependence on node leakage (node boundary conditions) whereas discontinuity factors have a weak dependence on burnup and a

strong dependence on leakage. This can be seen in table 7, which shows the change in discontinuity factor and homogenized thermal absorption cross section between the first and final iteration for node 2 in configuration 5.

Table 7 - Effect of Iterations on Thermal Absorption Cross Section and Discontinuity Factors

Iterations – Node 2					
Σ_a (Thermal)		Discontinuity factor (left)		Discontinuity factor (right)	
1 st iteration	15 th iteration	1 st iteration	15 th iteration	1 st iteration	15 th iteration
1.697 E-02	1.693E-01	0.9137	0.8555	0.9137	0.9886

When exact cross sections are used without discontinuity factors, the solution changes little from the standard-homogenization case because the cross sections do not change appreciably. Similarly, the solution changes little when discontinuity factors are calculated for the correct burnup using approximate, reflective, boundary conditions. Since there is very little change in discontinuity factors from one node to the next, the discontinuity condition expressed by Eq. (25) is very nearly a continuity condition. It follows that the use of RBC discontinuity factors brings only very little change compared to the standard-homogenization solution. The only way to obtain a strong improvement in accuracy is to correct both cross sections and discontinuity factors for leakage.

In all configurations, the thermal flux calculated by the iterative method can be seen to diverge from the reference case in the area of the eleventh (reflector) node. This is

likely due to the fact that the discontinuity factor applied to this node is set to unity, instead of being calculated through the iterations as for the remaining nodes. The actual discontinuity factors for the left side of the reflector node, as calculated from the reference case results, are 2.3 and 1.4 for the fast and thermal flux, respectively. The fast and thermal group discontinuity factors for the right side of the reflector node are 0.12 and 0.17, respectively. These values were found to be the same within one decimal point for all configurations. Thus, the use of unity for the reflector node discontinuity factors can be anticipated to cause error in the iterative method calculation results. Since, as explained previously, reflector-node discontinuity factors cannot be updated the same way as fuel-node discontinuity factors can, namely using single-node eigenvalue calculations, allowing them to remain at unity is justified.

The node-averaged fast and thermal fluxes calculated by the iterative method converged in 8-15 iterations for all configurations, slightly more than the 10 iterations reported by Rahnema and Nichita (1997) for LWR configurations. Figure 25 illustrates the convergence process by showing the fission rate results for every third iteration in configuration 5.

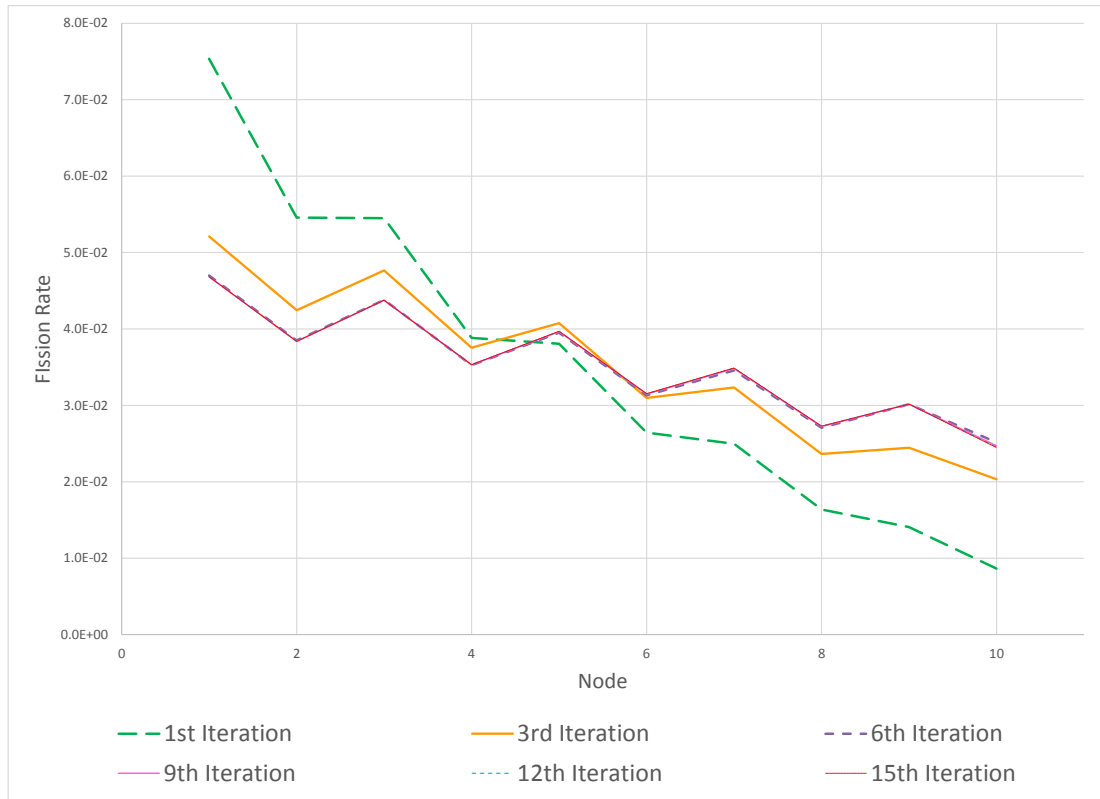


Figure 25 - Configuration 5 Fission Rate Results for Every Third Iteration.

The largest change in the calculated fission rate occurs after the first iteration. In the first iteration, the cross sections are not leakage-corrected and thus they correspond to the RBC assumption. There is little change observed between the ninth, twelfth, and fifteenth iteration, as the results have nearly converged to their final value at this point.

Overall, the results from the five test configurations show that using iterated leakage-corrected boundary conditions produce a significant improvement over RBC results for an 11-node model with PT-SCWR properties. The fast flux, thermal flux, fission rate, and k-effective value calculated using iterated boundary conditions are significantly better than those obtained through standard homogenization methods.

8 Conclusions and Future Work

The iterated method using GET and leakage correction shows promising results for PT-SCWR reactor physics calculations. Results based on reflective boundary conditions indicate large errors regardless of whether or not discontinuity factors are used. The issue encountered during implementation of the iterated method was difficulty in obtaining convergence with the diffusion code in the reflector node with a discontinuity factor applied. This is due to the fact that no fission source exists within the reflector node, which creates difficulty in solving the diffusion equation for that node.

Discontinuity factors were set to unity for the reflector node, which was seen to be a cause of larger error in that node. This was not a significant detriment to the results of the iterated method, as there is no power produced in the reflector node.

Based on the results obtained thus far, two directions for future investigations are recommended. The first direction is the development of a practical method to apply leakage corrections to the reflector-node discontinuity factors. The second direction is the extension of this work to two and three dimensional core models, as all configurations of practical interest are three-dimensional.

REFERENCES

Ackroyd, R.T., Gashut, A.M., and Abuzid, O.A., "Discontinuous variational solutions for the neutron diffusion equation", *Annals of Nuclear Energy*, **23**, 1289-1300 (1996).

Aragones, M. and Ahnert, C., "A linear discontinuous finite difference formulation for synthetic coarse-mesh few-group diffusion calculations", *Nuclear Science and Engineering*, **94**, 309 (1986).

Aragones, J.M., Ahnert, C., and Garcia-Herranz, N., "The analytic coarse-mesh finite difference method for multigroup and multidimensional diffusion calculations", *Nuclear Science and Engineering*, **157**, 1-15 (2007).

Berman, Y., "An improved homogenization technique for pin-by-pin diffusion calculations", *Annals of Nuclear Energy*, **53**, 238–243 (2013).

Chiang, R.T., "A lattice homogenization theory for coarse mesh diffusion analysis," ANS Conference on Advances in Reactor Physics and Thermal Hydraulics, Kiamesh Lake New York (1982).

Chow, C.K. and Khartabil, H.F., "Conceptual fuel channel designs for CANDU - SCWR" *Nuclear Engineering and Technology*, **40**, Special Issue on the 3rd International Symposium on SCWR (2007).

Clarno, K.T. and Adams, M.L., "Capturing the effects of unlike neighbors in single-assembly calculations", ANS Conference Proceedings, Gatlinburg Tennessee (2003).

Connolly, K.J. and Rahnema, F., "A heterogeneous coarse mesh radiation transport method for neutronic analysis of prismatic reactors", *Annals of Nuclear Energy*, **56**, 87–101 (2013).

Dahmani, M., Marleau, G., and Le Tellier, R., "Modeling reactivity devices for advanced CANDU reactors using the code DRAGON", *Annals of Nuclear Energy*, **35**, 804–812 (2008).

Dall'Osso, A., "A spatial rehomogenization method in nodal calculations", *Annals of Nuclear Energy*, **33**, 869–877 (2006).

Garcia-Herranz, N., Herrero, J.J., Cuervo, D., and Ahnert, C., "Interface discontinuity factors in the modal eigenspace of the multipgroup diffusion matrix", *International Conference on Mathematics and Computational Methods Applied to Nuclear Science and Engineering*, Brazil (2011).

Gomes, G., "Importance of assembly discontinuity factors in simulating reactor cores containing highly heterogeneous fuel assemblies", *Proceedings of the COMSOL Conference*, Boston (2009).

Han T.Y., Joo, H.G, Lee, H.C., and Kim, C.H., "Multi-group unified nodal method with two-group coarse-mesh finite difference formulation", *Annals of Nuclear Energy*, **35**, 1975–1985 (2008).

Hebert, A., "A consistent technique for the pin-by-pin homogenization of a pressurized water reactor assembly", *Nuclear Science and Engineering*, **113**, 227-238 (1993).

Henry, F. and Hoxie, C.L., "Reconstruction of heterogeneous PWR flux shapes from nodal calculations", *Transaction of the American Nuclear Society*, **39**, 905 (1981).

Herrero, J.J, Garcia-Herranz, N., Cuervo, D., and Ahnert, C., "*Annals of Nuclear Energy*, **46**, 106–115 (2012).

Jagannathan, V., Mohanakrishnan, P., Menon, S.V.G., Srinivasan, K.R., and Rastogi, B.P., "An Assessment of the BWR fuel box-lattice-cell homogenization procedures with the tarapur BWR incore and excore measurements", *Annals of Nuclear Energy*, **10**, 339-350 (1983).

Kim, R. and Cho, N.Z., "Global/local iterative methods for equivalent diffusion theory parameters in nodal calculation", *Annals of Nuclear Energy*, **20**, 767-783 (1993).

Kim, K.S. and DeHart, M.D., "Unstructured partial- and net-current based coarse mesh finite difference acceleration applied to the extended step characteristics method in NEWT", *Annals of Nuclear Energy*, **38**, 527–534 (2011).

Koebke, K., “A new approach to homogenization and group condensation”, Technical Committee Meeting on Homogenization Methods in Reactor Physics, Lugano Switzerland (1978).

Kozlowski, T., “Cell Homogenization Method for Pin-by-Pin Neutron Transport Calculations”, *Nuclear Science and Engineering*, **169**, 1–18 (2011).

Lawrence, R.D., “Progress in nodal methods for the solution of the neutron diffusion and transport equations”, *Progress in Nuclear Energy*, **17**, 271-301 (1986).

Leszczynski, F., Lopez Aldama, D., and Trkov, A., “WIMS-D library update”, IAEA, Vienna Austria (2007).

Lorberg, J., Österlund, M., Bejmer, K., Blomgren, J., and Kierkegaard, J., “Homogenization of cross sections and computation of discontinuity factors for a real 3-D BWR bottom reflector for comparison with lattice and nodal codes”, *Nuclear Technology*, **177** (2012).

Marleau, G., Hébert, A., and Roy, R., “A User Guide for DRAGON 3.05E”, École Polytechnique de Montréal (2007).

Marleau, G., Hébert, A., and Roy, R., “A User Guide for DRAGON 3.06”, Technical Report IGE-174 Rev.10, École Polytechnique de Montréal (2012).

McDonald, M.H., “Fuel and Core Physics Considerations for a Pressure Tube Supercritical Water Cooled Reactor”, *McMaster University Open Access Dissertations and Theses*, Paper 6207 (2011).

Merk, B. and Rohde, U., “An analytical solution for the consideration of the effect of adjacent fuel elements”, *Annals of Nuclear Energy*, **38**, 2428–2440 (2011).

Nakahara, Y., Suyama, K., Inagawa, J., Nagaishi, R., Kurosawa, S., Kohno, N., Onuki, M., and Mochizuki, H., “Nuclide composition benchmark data set for verifying burnup codes on spent light water reactor fuels”, *Nuclear Technology*, **137**, 111 (2002).

Nichita, E., "Evaluation of the need for discontinuity factors for neutronic modelling of CANDU low-void reactivity fuel lattices", Proceedings 9th International Conference on CANDU Fuel, Belleville Ontario Canada (2005).

Nichita, E., "Evaluating accuracy of standard homogenization and need for generalized equivalence theory for ACR-lattice checkerboard configurations", Annals of Nuclear Energy, **36**, 760–766 (2009).

Nichita, E., Zabienski, K., and Gravel, M., "A three-dimensional two-energy-group finite-difference neutron-diffusion code with discontinuity factors", Proceedings 28th Annual Conference of the Canadian Nuclear Society, New Brunswick (2007).

Ott, K.O. and Bezella, W.A., *Introductory Nuclear Reactor Statics*, La Grange Park: American Nuclear Society, (1989). Print.

Pomraning, C., "Variational principle for eigenvalue equations", Journal of Mathematical Physics, **8**, 149-158 (1967).

Rahnema, F., "Boundary Condition Perturbation Theory for use in Spatial Homogenization Methods", Nuclear Science and Engineering, **102**, 183-190 (1989).

Rahnema, F. and McKinley, M.S., "High-order cross-section homogenization method", Annals of Nuclear Energy, **29**, 875–899 (2002).

Rahnema, F. and Nichita, E., "Leakage corrected spatial (assembly) homogenization technique", Annals of Nuclear Energy, **24**, 477-488 (1997).

Sanchez, R., "Assembly homogenization techniques for core calculations", Progress in Nuclear Energy, **51**, 14-31 (2009).

Shen, W., "Assessment of the traditional neutron-diffusion core-analysis method for the analysis of the Super Critical Water Reactor", Annals of Nuclear Energy, **45**, 1–7 (2012a).

Shen, W., "On the better performance of the coarse-mesh finite-difference method for CANDU-type reactors", Annals of Nuclear Energy, **46**, 169–178 (2012b).

Smith, K.S., "Spatial homogenization methods for light water reactor analysis", Ph.D Thesis, MIT (1980).

Smith, K.S., "Assembly homogenization techniques for light water reactor analysis", *Progress in Nuclear Energy*, **17**, 303-335 (1986).

Smith, K.S., "Practical and efficient iterative method for LWR fuel assembly homogenization", *Transactions of the American Nuclear Society*, **71**, 13-18 (1994).

Yamamoto, A., "Analytic derivation of the correction factor for the improved coarse mesh method", *Annals of Nuclear Energy*, **31**, 71–86 (2004).

Yamamoto, A., Kitamura, Y., and Yamane, Y., "Cell homogenization methods for pin-by-pin core calculations tested in slab geometry", *Annals of Nuclear Energy*, **31**, 825–847 (2004).

Yetisir, M., Diamond, W., Leung, L.K.H., Martin, D., and Duffey, R., "Conceptual Mechanical Design for a Pressure-Tube Type Supercritical Water-Cooled Reactor", *Proceedings of the 5th International Symposium on SCWR*, Paper 055 (2011).

Zhang, D. and Rahnema, F., "An efficient hybrid stochastic/deterministic coarse mesh neutron transport method", *Annals of Nuclear Energy*, **41**, 1–11 (2012).